理學碩士 學位 論文

Atomic-level investigation

of molecular behaviors on solid surface

(원자 수준에서의 고체 표면 위 분자 거동 연구)

蔚 山 大 學 校 大 學 院

化 學 科

李 民 喜

Atomic-level investigation

of molecular behaviors on solid surface

指 導 敎 授 정 재 훈

이 論文을 理學碩士 學位 論文으로 제출함

2019年 8月

蔚 山 大 學 校 大 學 院

化 學 科

李 民 喜

李 民 喜의 理學碩士 學位 論文을 認准함

審査委員　　강 성 구

審査委員　　고 원 석

審査委員　　정 재 훈

蔚 山 大 學 校 大 學 院

2019年　8月

Contents

1. Introduction

Chemical reactions on surfaces which called 'surface chemistry' have been studied, and it is important to comprehend the mechanism of the reaction and clarify the relationship between reactant and surface to improve the model systems. It is general to use the surface as a catalyst or to manipulate the physical/chemical properties of the surface for utilizing in industry. In order to increase the reactivity of the catalyst and induce the reaction in the desired direction, it is necessary to figure out the surface properties and find the driving force of the reaction. Reactions taking place on the surface are difficult to analyze accurately because there are various factors that affect on the reaction pathway. Moreover, the precise investigation in an atomic-level was impossible in the past. With the development of scanning probe microscopy (SPM) and computational method, it is able to study real-space investigation. These two approaches were used to understand in-depth and provide insight into mechanism analysis. In this study, we demonstrate a fundamental study for controlling the reactivity and proposed reliable surface-reactant relationships.

1.1. Computational study on OH-Gr/Cu(111)

The OH-Gr with $(\sqrt{3}\times\sqrt{3})R30°$ superstructure observed in STM experiments is thermodynamically more stable and also has a lower activation energy than other ordered configurations. I am investigating the formation mechanism of highly-ordered hydroxylated graphene (OH-Gr) epitaxially-grown on Cu(111) substrate using DFT calculations (Figure 1.1a). I figure out that kinetically favored OH adsorption configuration and this is determined with the balance between H-bonding and OH-Gr/Cu(111) interaction. This handle on section 3.1. Highly-ordered hydroxylation on graphene/Cu(111).

1.2. Experimental study on O₂/Ag(110)

In the experimental study, I study dissociation of a single O_2 molecule on Ag(110). Understanding the dissociation of O_2 molecule is important because this is a crucial reaction as the first step of oxidation in catalytic industry such as epoxidation. However, previous studies describe chemisorbed O_2 species and dissociation without interpretation for an exact mechanism. I observed two orientations; O_2[1-10] and O_2[001] (Figure 1.1b) and investigate the reaction behaviors of O_2 induced by injecting tunneling electrons or holes from the STM tip. I have found not only dissociation (Figure 1.1b) but also rotation and hopping are induced by electrons and holes, which was not reported formerly. Now, this study is ongoing to reveal the details of the reaction pathway. It is explained in detail on section 3.2. Electron-induced O2 dissociation on Ag(110).
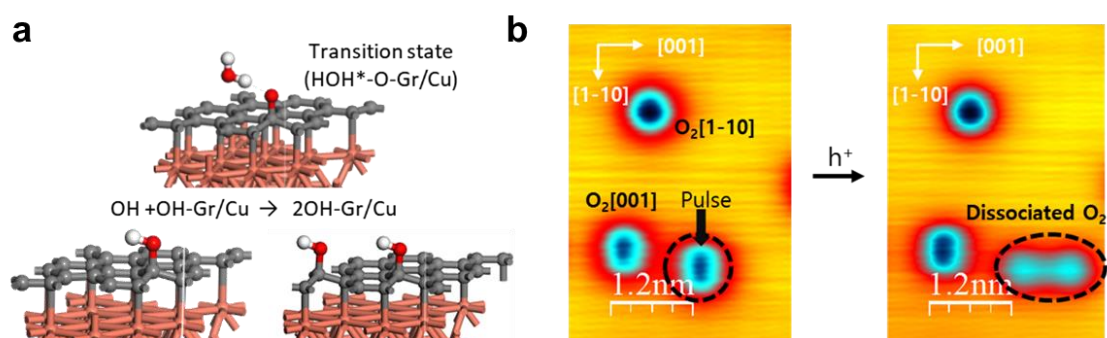

Figure 1.1. (a) Second OH adsorption reaction mechanism. (b) Two adsorbed O_2 species on Ag(110) and dissociation of O_2.

2. Methodological background: DFT & STM

Modern density functional theory plays an important role in many fields of science. The main research strategy of this thesis is the computational method based on the density functional theory and STM experiment, which was extensively used to explain various surface phenomena such as adsorption and chemical reactions. In this Chapter, the essentials of electronic structure theory are briefly summarized to provide theoretical background from the Schrödinger equation for many-body system to Kohn-Sham density functional equation.[1-3] The mathematical notations used in this Chapter are mainly based on the book written by Richard M. Martin, "Electronic Structure: Basic Theory and Practical Methods".[1] A simple introduction to scanning tunneling microscopy is provided at the last section.[4]

2.1. The Schrodinger equation for many-body electron systems

2.1.1. The Born-Oppenheimer approximation

The fundamental Hamiltonian for a system of interacting electrons and nuclei is

$$\hat{H} = -\frac{\hbar^2}{2m_e}\sum_i \nabla_i^2 - \sum_{i,I}\frac{Z_I e^2}{\left|\mathbf{r}_i - \mathbf{R}_I\right|} + \frac{1}{2}\sum_{i\neq j}\frac{e^2}{\left|\mathbf{r}_i - \mathbf{r}_j\right|} - \sum_I \frac{\hbar^2}{2M_I}\nabla_I^2 + \frac{1}{2}\sum_{I\neq J}\frac{Z_I Z_J e^2}{\left|\mathbf{R}_I - \mathbf{R}_J\right|} \tag{2.1}$$

where electrons are denoted by lower case subscripts and nuclei, with charge Z_I, mass M_I, and position R_I, denoted by upper case subscripts. If we first set the mass of the nuclei to infinity, then the nuclear kinetic energy can be ignored, which means that the motions of electrons and nuclei can be decoupled and treated separately. This is the Born-Oppenheimer or adiabatic approximation.[5] Thus, we shall focus on the Hamiltonian for the electrons, where the positions of the nuclei are parameters.

Ignoring the nuclear kinetic energy, the fundamental Hamiltonian for the theory of electronic structure can be written as

$$\hat{H} = \hat{T} + \hat{V}_{ext} + \hat{V}_{int} + E_{II} , \tag{2.2}$$

If we adopt Hartree atomic units $\hbar = m_e = e = 4\pi/\varepsilon_0 = 1$, then each term of the Hamiltonian (2.1) can be written in its simplest form. The kinetic energy operator for the electrons $\hat{T}$ is

$$\hat{T} = -\frac{1}{2} \sum_i \nabla_i^2 , \tag{2.3}$$

$\hat{V}_{ext}$ is the potential acting on the electrons due to the nuclei,

$$\hat{V}_{ext} = \sum_{i,I} V_I \left(|\mathbf{r}_i - \mathbf{R}_I| \right) , \tag{2.4}$$

$\hat{V}_{int}$ is the electron-electron interaction,

$$\hat{V}_{int} = \frac{1}{2} \sum_{i \neq j} \frac{1}{|\mathbf{r}_i - \mathbf{r}_j|} , \tag{2.5}$$

and the final term E_{II} is the nuclear repulsion energy, the classical interaction of nuclei with one another, which can be treated as additive terms in electronic structures theory. The interaction of the nuclei with the electrons is considered as a fixed potential "external" to electrons. Therefore, the Hamiltonian (2.2) provides an excellent starting point in electronic structure theory including various external potentials, such as electric fields and Zeeman terms.

2.1.2. The Schrodinger equation for many-body electron systems

For non-relativistic quantum systems, the fundamental equation describing a temporal evolution is the time-dependent Schrödinger equation,

$$i\hbar \frac{d\Psi(\{\mathbf{r}_i\};t)}{dt} = \hat{H}\Psi(\{\mathbf{r}_i\};t) , \tag{2.6}$$

where the many-body wavefunction for the electron is $\Psi(\{\mathbf{r}_i\};t) \equiv \Psi(\mathbf{r}_1, \mathbf{r}_2, \cdots, \mathbf{r}_N; t)$. The eigenstates can be written as $\Psi(\{\mathbf{r}_i\};t) \equiv \Psi(\{\mathbf{r}_1\})e^{-i(E/\hbar)t}$. This is the basis for understanding dynamical properties of a non-relativistic quantum system.

However, for systems in a stationary state, it can be governed by the time-independent Schrödinger equation,

$$\hat{H} \mid \Psi\rangle = E \mid \Psi\rangle .$$
(2.7)

Any observables in time-independent expression can be obtained as an expectation value of an operator $\hat{O}$, which involves an integral over all coordinates,

$$\langle \hat{O} \rangle = \frac{\langle \Psi \mid \hat{O} \mid \Psi\rangle}{\langle \Psi \mid \Psi\rangle} .$$
(2.8)

Thus, the total energy is the expectation value of the Hamiltonian,

$$E = \frac{\langle \Psi \mid \hat{H} \mid \Psi\rangle}{\langle \Psi \mid \Psi\rangle} \equiv \langle \hat{H} \rangle = \langle \hat{T} \rangle + \langle \hat{V}_{\text{int}} \rangle + \int \mathrm{d}^3 r V_{\text{ext}}(\mathbf{r})n(\mathbf{r}) + E_{II}$$
(2.9)
,

where the expectation value of the external potential has been explicitly written as a simple integral over the density function. The density of particle $n(\mathbf{r})$ is given by the expectation value of the density operator $\hat{n}(\mathbf{r}) = \sum_{i=1,N} \delta(\mathbf{r} - \mathbf{r}_i)$.

Considering the energies in extended systems with long-range Coulomb interaction, the energy (2.9) can be written as

$$E = \langle \hat{T} \rangle + (\langle \hat{V}_{\text{int}} \rangle - E_{\text{Hartree}}) + E^{CC} ,$$
(2.10)

where the classical Coulomb energies are can be defined by

$$E^{CC} = E_{\text{Hartree}} + \int \mathrm{d}^3 r V_{\text{ext}}(\mathbf{r})n(\mathbf{r}) + E_{II} ,$$
(2.11)

and E_{Hartree} is the self-interaction energy of the density $n(\mathbf{r})$ treated as a classical charge density

$$E_{\text{Hartree}} = \frac{1}{2} \int d^3 r d^3 r' \frac{n(\mathbf{r})n(\mathbf{r}')}{|\mathbf{r} - \mathbf{r}'|} \tag{2.12}$$

Since E_{II} is the interaction among the nuclei and $\int d^3 r V_{\text{ext}}(\mathbf{r})n(\mathbf{r}')$ is the interaction of the electrons with the nuclei, the energy (2.10) is organized in neutral groups so long as the system is neutral.

The ground state wavefunction $\Psi 0$ is the state with lowest energy, which can be determined, in principle, by minimizing the total energy with respect to all the parameters in $\Psi(\{\mathbf{r}_i\})$, with the constraint that Ψ must obey the particle symmetry and any conservation laws. Excited states are saddle points of the energy with respect to variation in Ψ.

2.1.3. Hartree-Fock approximation

The standard method in many-particle theory is the Hartree-Fock method.[6] In this approach, the main advantage is that the many-electron Schrödinger equation can be treated with many simple one-electron equations.

If there is no spin-orbital interaction, the Slater determinant can be given as

$$\Phi = \frac{1}{\sqrt{N!}} \begin{vmatrix} \phi_1(\mathbf{r}_1,\sigma_1) & \phi_1(\mathbf{r}_2,\sigma_2) & \cdots & \phi_1(\mathbf{r}_N,\sigma_N) \\ \phi_2(\mathbf{r}_1,\sigma_1) & \phi_2(\mathbf{r}_2,\sigma_2) & \cdots & \phi_2(\mathbf{r}_N,\sigma_N) \\ \phi_3(\mathbf{r}_1,\sigma_1) & \phi_3(\mathbf{r}_2,\sigma_2) & \cdots & \phi_3(\mathbf{r}_N,\sigma_N) \\ \vdots & \vdots & \ddots & \vdots \\ \phi_N(\mathbf{r}_1,\sigma_1) & \phi_N(\mathbf{r}_2,\sigma_2) & \cdots & \phi_N(\mathbf{r}_N,\sigma_N) \end{vmatrix} \tag{2.13}$$

where the $\phi_i(\mathbf{r}_j,\sigma_j)$ are single particle "spin-orbitals" each of which is a product of a function of the position $\psi_i^\sigma(\mathbf{r}_j)$ and a function of the spin variable $\alpha_i(\sigma_j)$.[7] The one-electron function determined from the Slater determinant must be antisymmetric with respect to the interchange of any two electron coordinates because electrons are fermions

which have a spin of 1/2. The Pauli principle, which states that two electrons cannot have all quantum numbers equal, is a direct consequence of this antisymmetric requirement. In addition, the spin-orbitals can be taken to be linearly independent, i.e., orthonormal.

Furthermore, if the Hamiltonian is independent of spin, the expectation value of the Hamiltonian (2.2) with the wavefunction, determined by the Slater determinant, is

$$
\begin{aligned}
E = \langle \Phi | \hat{H} | \Phi \rangle = \sum_{i,\sigma} \int d\mathbf{r}\, \psi_i^{\sigma*}(\mathbf{r}) \left[-\frac{1}{2}\nabla^2 + V_{\text{ext}}(\mathbf{r}) \right] \psi_i^{\sigma}(\mathbf{r}) + E_{II} \\
+ \frac{1}{2} \sum_{i,j,\sigma_i,\sigma_j} \int d\mathbf{r}d\mathbf{r}'\, \psi_i^{\sigma_i*}(\mathbf{r}) \psi_j^{\sigma_j*}(\mathbf{r}') \frac{1}{|\mathbf{r}-\mathbf{r}'|} \psi_i^{\sigma_i}(\mathbf{r}) \psi_j^{\sigma_j}(\mathbf{r}') \, . \\
- \frac{1}{2} \sum_{i,j,\sigma} \int d\mathbf{r}d\mathbf{r}'\, \psi_i^{\sigma*}(\mathbf{r}) \psi_j^{\sigma*}(\mathbf{r}') \frac{1}{|\mathbf{r}-\mathbf{r}'|} \psi_j^{\sigma}(\mathbf{r}) \psi_i^{\sigma}(\mathbf{r}') \, .
\end{aligned}
\tag{2.14}
$$

The first and second terms are one-electron expectation values which involve a sum over orbitals and with respect to the one-electron operator and nuclear repulsion energy, whereas the third and fourth terms are the Coulomb and exchange interactions among electrons which involve two electron integrals with respect to Coulomb and exchange operators, respectively. The "Coulomb" term represents a classical electrostatic repulsion between two charge distributions. The "exchange" term, which does not have a classical analogy, only acts between same spin electrons since the spin parts of the orbitals are orthogonal for opposite spins.

The Hartree-Fock approach is to minimize the total energy with respect to all degrees of freedom in the wavefunction with the restriction of the Slater determinant. The orthonormality is maintained during minimization by the Lagrange multiplier. If the spin functions are quantized along an axis, a variation of $\psi_i^{\sigma*}(\mathbf{r})$ for each spin σ leads to the Hartree-Fock equations

$$
\begin{aligned}
\left[-\frac{1}{2}\nabla^2 + V_{\text{ext}}(\mathbf{r}) + \sum_{j,\sigma_j} \int d\mathbf{r}'\, \psi_j^{\sigma_j*}(\mathbf{r}') \psi_j^{\sigma_j}(\mathbf{r}') \frac{1}{|\mathbf{r}-\mathbf{r}'|} \right] \psi_i^{\sigma}(\mathbf{r}) \\
- \sum_j \int d\mathbf{r}'\, \psi_j^{\sigma*}(\mathbf{r}') \psi_i^{\sigma*}(\mathbf{r}') \frac{1}{|\mathbf{r}-\mathbf{r}'|} \psi_j^{\sigma}(\mathbf{r}) = \varepsilon_i^{\sigma} \psi_i^{\sigma}(\mathbf{r}),
\end{aligned}
\tag{2.15}
$$

where the exchange term is summed over all orbitals of the same spin including the self-term $i = j$. If the exchange term is modified by multiplying and dividing by $\psi_i^\sigma(\mathbf{r})$, Hartree-Fock equations (2.15) can be written using effective Hamiltonian, i.e. Fock operator, as

$$\hat{H}_{\text{eff}}\psi_i^\sigma(\mathbf{r}) = \left[-\frac{\hbar^2}{2m_e}\nabla^2 + \hat{V}_{\text{eff}}^{i,\sigma}(\mathbf{r})\right]\psi_i^\sigma(\mathbf{r}) = \varepsilon_i^\sigma\psi_i^\sigma(\mathbf{r}),\tag{2.16}$$

with

$$\hat{V}_{\text{eff}}^{i,\sigma}(\mathbf{r}) = V_{\text{ext}}(\mathbf{r}) + V_{\text{Hartree}}(\mathbf{r}) + \hat{V}_x^{i,\sigma}(\mathbf{r}),\tag{2.17}$$

and the exchange term operator $\hat{V}_x^{i,\sigma}(\mathbf{r})$ is given by a sum over orbitals of the same spin σ,

$$\hat{V}_x^{i,\sigma}(\mathbf{r}) = -\sum_j \int d\mathbf{r}'\,\psi_j^{\sigma*}(\mathbf{r}')\psi_j^\sigma(\mathbf{r}')\frac{1}{|\mathbf{r}-\mathbf{r}'|}\frac{\psi_j^\sigma(\mathbf{r})}{\psi_i^\sigma(\mathbf{r})}.\tag{2.18}$$

The Lagrange multipliers ε_i^σ can be interpreted as the expectation value of the Fock operator. In general, a basis set must be used to solve Hartree-Fock equations, where the energy (2.14) can be written in terms of the expansion coefficients of the orbitals and the integrals involving basis functions. A specific Fock orbital can only be determined if all the other occupied orbitals are known, and iterative methods must therefore be employed for determining the orbitals. A set of functions, solution of Hartree-Fock equations (2.16), is called Self-Consistent Field (SCF) orbitals. The electron-electron repulsion is only accounted for in an average fashion, and the Hartree-Fock method is therefore also referred to as a Mean Field approximation.

The key problem of electronic structure is that the electrons form an interacting many-body system. Since the interactions always involve pairs of electrons, two-body correlation functions are sufficient to determine many properties, such as the energy given by (2.9). The joint probability $n(\mathbf{r},\sigma;\mathbf{r}',\sigma')$ of finding electrons of spin σ at point $\mathbf{r}$ and of spin σ' at point $\mathbf{r}'$, is given by

$$n(\mathbf{r}, \sigma; \mathbf{r}', \sigma') = \left\langle \sum_{i \neq j} \delta(\mathbf{r} - \mathbf{r}_i) \delta(\sigma - \sigma_i) \delta(\mathbf{r}' - \mathbf{r}_j) \delta(\sigma' - \sigma_j) \right\rangle, \quad (2.19)$$

assuming Ψ is normalized to unity. For uncorrelated particles, the joint probability is just the product of probabilities, so that the measure of correlation is $\Delta n(\mathbf{r}, \sigma; \mathbf{r}', \sigma') = n(\mathbf{r}, \sigma; \mathbf{r}', \sigma') - n(\mathbf{r}, \sigma) n(\mathbf{r}', \sigma')$. Physically, electron correlation corresponds to the motion of the electrons being correlated; on average they are farther apart than described by the Hartree-Fock wave function. Since the correlation between opposite spins has both intra- and inter-orbital contributions, it will be larger than the correlation between electrons having the same spin. The opposite spin correlation is called the Coulomb correlation, while the same spin correlation is called Fermi correlation.

The Hartree-Fock approximation (HFA) neglects all correlations except those required by the Pauli exclusion principle. Therefore, the improvement of the wavefunction to include correlation introduces extra degrees of freedom in the wavefunction and therefore always lowers the energy for any state. The lowering of the energy is termed "correlation energy" E_c. It is often very important for describing chemical phenomena. Since E_{HFA} is the lowest possible energy neglecting correlation, the definition of correlation energy in terms of the difference from the Hartree-Fock approximation is a well-defined choice. To consider the correction of correlation energy, there are a number of types of calculations: Møller-Plesset (MP) perturbation theory, Configuration Interaction (CI) and Coupled Cluster (CC) methods.[2,3,8-10] In addition to the traditional ab-initio electron correlation method, Density Functional Theory (DFT) has become very popular in recent years.[11,12] Electron density is used to obtain energy, which is a three-dimensional function, thus scaling as N^3. Furthermore, at least some electron correlation can be included in the calculation.

2.2. Density functional theory

2.2.1. Hohenberg-Kohn theorems

In the fundamental philosophy of DFT, all properties of a system composed of many interacting particles can be determined by a ***functional*** of the ground state electron

density $n_0(\mathbf{r})$. This is based upon the theorems for such functionals as given by   P. Hohenberg and W. Kohn in 1964.[13]

- **Theorem I**: *For any system of interacting particles in an external potential $V_{ext}(\mathbf{r})$, the potential $V_{ext}(\mathbf{r})$ is determined uniquely, except for a constant, by the ground state particle density $n_0(\mathbf{r})$.*

Therefore, if the Hamiltonian is uniquely determined by the ground state density $n_0(\mathbf{r})$ according to the Hohenberg-Kohn theorem I, the wavefunction of any state can be determined by solving the Schrödinger equation with this Hamiltonian. Thus, all properties of the system are completely determined by ground state density.

- **Theorem II**: *A universal functional for the energy $E[n]$ in terms of the density $n(\mathbf{r})$ can be defined, valid for any external potential $V_{ext}(\mathbf{r})$. For any particular $V_{ext}(\mathbf{r})$, the exact ground state energy of the system is the global minimum value of this functional, and the density $n(\mathbf{r})$ that minimizes the functional is the exact ground state density $n_0(\mathbf{r})$.*

Therefore, if the functional including all internal energies (kinetic and potential energies) of the interacting electron system is known, the exact ground state density of energy by minimizing the total energy of the system using the variational principle with respect to the density function $n(\mathbf{r})$. However, the Hohenberg-Kohn theorem II does not provide any guidance concerning the excited states of the electrons.

2.2.2. The Kohn-Sham approach

The Kohn-Sham approach is to replace the difficult interacting many-body system with a different auxiliary system which can be more easily solved. The *ansatz* of Kohn and Sham assumes that the ground state density of the original interacting system is equal to that of some chosen non-interacting system.[11,12] This leads to independent-particle equations for the non-interacting system that can be considered exactly soluble with all the difficult many-body terms incorporated into an exchange-correlation functional of the density. Therefore, the accuracy of Kohn-Sham approach is only limited by the exchange-correlation functional.

The Kohn-Sham construction of an auxiliary system rests upon two assumptions: (1) The exact ground state density can be represented by the ground state density of an auxiliary system of non-interacting particles. This leads to the relation of the actual and auxiliary systems. (2) The auxiliary Hamiltonian is chosen to have the usual kinetic operator and an effective local potential $V_{\mathrm{eff}}^{\sigma}(\mathbf{r})$ acting on an electron of spin σ at point $\mathbf{r}$.

The auxiliary Hamiltonian for the independent-particle system is

$$\hat{H}_{\mathrm{aux}}^{\sigma} = -\frac{1}{2}\nabla^2 + V^{\sigma}(\mathbf{r}). \tag{2.20}$$

The density of the auxiliary system is given by sums of squares of the orbitals for each spin

$$n(\mathbf{r}) = \sum_{\sigma} n(\mathbf{r},\sigma) = \sum_{\sigma}\sum_{i=1}^{N^{\sigma}}\left|\psi_i^{\sigma}(\mathbf{r})\right|^2, \tag{2.21}$$

the independent-particle kinetic energy T_s is given by

$$T_s = -\frac{1}{2}\sum_{\sigma}\sum_{i=1}^{N^{\sigma}}\left\langle\psi_i^{\sigma}\left|\nabla^2\right|\psi_i^{\sigma}\right\rangle = \frac{1}{2}\sum_{\sigma}\sum_{i=1}^{N^{\sigma}}\int d^3 r\left|\nabla\psi_i^{\sigma}(\mathbf{r})\right|^2, \tag{2.22}$$

and we define the classical Coulomb interaction energy of the electron density $n(\mathbf{r})$ interacting with itself, i.e., the Hartree energy

$$E_{\mathrm{Hartree}}[n] = \frac{1}{2}\int d^3 r d^3 r'\frac{n(\mathbf{r})n(\mathbf{r}')}{\left|\mathbf{r}-\mathbf{r}'\right|}. \tag{2.23}$$

The [n] denotes a functional of the density $n(\mathbf{r},\sigma)$ which depends on both position in space $\mathbf{r}$ and spin σ. Now, the Kohn-Sham approach to the full interacting many-body problem is to rewrite the Hohenberg-Kohn expression for the ground state energy functional in the form

$$E_{\mathrm{KS}} = T_s[n] + \int d\mathbf{r} V_{\mathrm{ext}}(\mathbf{r})n(\mathbf{r}) + E_{\mathrm{Hartree}}[n] + E_{II} + E_{\mathrm{xc}}[n]. \tag{2.24}$$

Here, all many-body effects of exchange of correlation are grouped into the exchange-correlation energy E_{xc}.

$$E_{xc}[n] = \left\langle \hat{T} \right\rangle - T_s[n] + \left\langle \hat{V}_{int} \right\rangle - E_{Hartree}[n] .\qquad(2.25)$$

If the universal functional $E_{xc}[n]$ defined in (2.25) were known, then the exact ground state energy and density of the many-body electron problem could be found by self-consistently solving the Kohn-Sham equations for independent particles.

The Kohn-Sham auxiliary system for the ground state can be viewed as a problem of minimization with respect to density $n(\mathbf{r},\sigma)$. Because T_s is the functional of the orbitals and all other terms are functionals of the density, one can vary the wavefunctions and use the chain rule to derive the variational equation

$$\frac{\delta E_{KS}}{\delta \psi_i^{\sigma*}(\mathbf{r})} = \frac{\delta T_s}{\delta \psi_i^{\sigma*}(\mathbf{r})} + \left[\frac{\delta E_{ext}}{\delta n(\mathbf{r},\sigma)} + \frac{\delta E_{Hartree}}{\delta n(\mathbf{r},\sigma)} + \frac{\delta E_{xc}}{\delta n(\mathbf{r},\sigma)} \right] \frac{\delta n(\mathbf{r},\sigma)}{\delta \psi_i^{\sigma*}(\mathbf{r})} = 0 ,\qquad(2.26)$$

subject to the orthonormalization constraints

$$\left\langle \psi_i^{\sigma} \middle| \psi_j^{\sigma'} \right\rangle = \delta_{i,j}\delta_{\sigma,\sigma'} .\qquad(2.27)$$

Using expressions (2.21) and (2.22) for $n^{\sigma}(\mathbf{r})$ and T_s, which give

$$\frac{\delta T_s}{\delta \psi_i^{\sigma*}(\mathbf{r})} = -\frac{1}{2}\nabla^2 \psi_i^{\sigma}(\mathbf{r}) \; ; \frac{\delta n(\mathbf{r},\sigma)}{\delta \psi_i^{\sigma*}(\mathbf{r})} = \psi_i^{\sigma}(\mathbf{r}) ,\qquad(2.28)$$

and using the Lagrange multiplier method leads to Kohn-Sham Schrödinger-like equations:

$$\left(H_{KS}^{\sigma} - \varepsilon_i^{\sigma} \right)\psi_i^{\sigma}(\mathbf{r}) = 0 ,\qquad(2.29)$$

where ε_i are the eigenvalues, and H_{KS} is the effective Hamiltonian

$$H_{KS}^{\sigma} = -\frac{1}{2}\nabla^2 + V_{KS}^{\sigma}(\mathbf{r}),$$
(2.30)

with

$$V_{KS}^{\sigma}(\mathbf{r}) = V_{ext}(\mathbf{r}) + \frac{\delta E_{Hartree}}{\delta n(\mathbf{r},\sigma)} + \frac{\delta E_{xc}}{\delta n(\mathbf{r},\sigma)} = V_{ext}(\mathbf{r}) + V_{Hartree}(\mathbf{r}) + V_{xc}^{\sigma}(\mathbf{r}).$$
(2.31)

Kohn-Sham equations have the form of independent particle equations with a potential that must be solved self-consistently with the resulting energy or Hellmann-Feynman force. (The typical iterative process is shown in Figure 2.1.) These equations would lead to the exact ground state density and energy for the interaction system, if the exact functional $E_{xc}[n]$ were known. Therefore, the major problem in DFT is deriving suitable formulas for the exchange-correlation term.

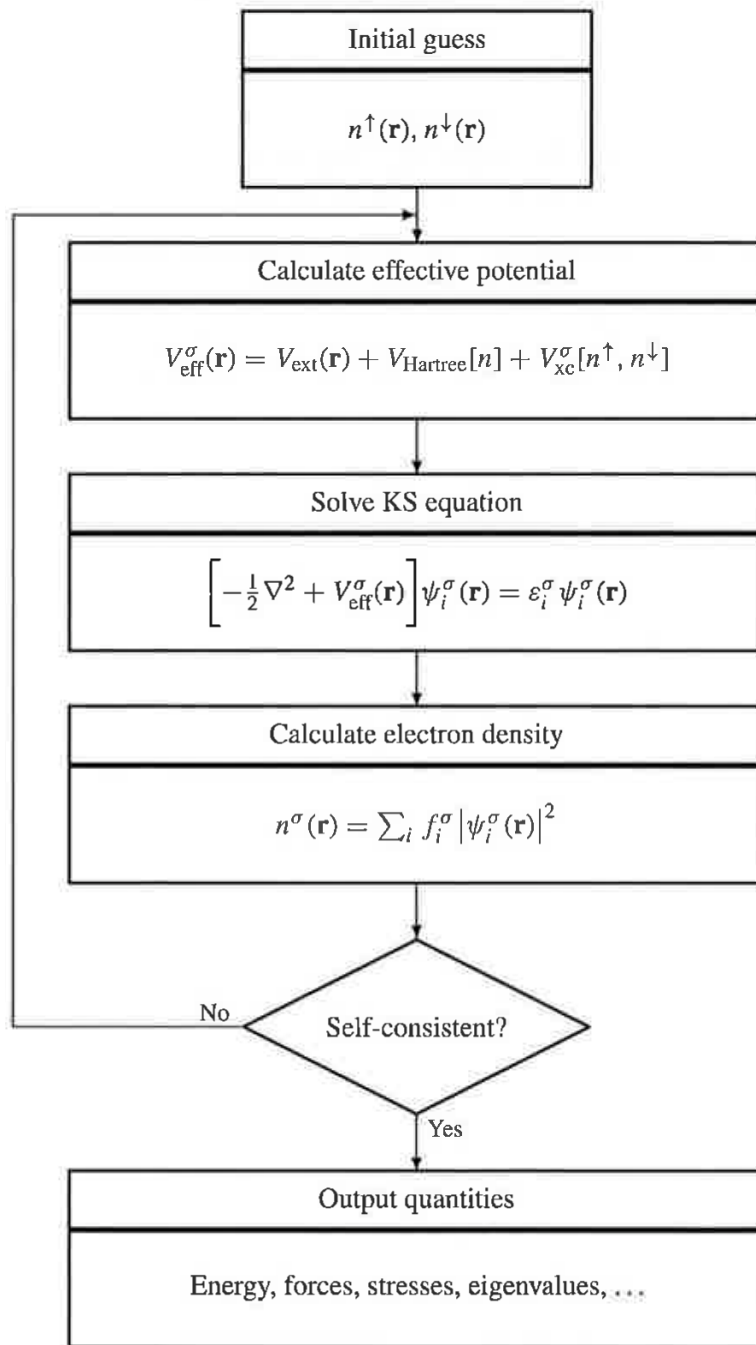**Figure 2.1.** Schematic representation of the self-consistent loop for solution of Kohn-Sham equations. [Adapted from Reference 1]

2.2.3. The exchange-correlation functional

In the practical use of DFT, the most general approximations to describe $E_{xc}[n]$ are local density approximation (LDA) (or more generally, the local spin density approximation (LSDA)) and generalized gradient approximation (GGA).

Usually solids can be considered as close to the limit of the homogeneous electron gas. In that limit, the effects of exchange and correlation are local in character. Therefore, in the case of LDA, the exchange-correlation energy is simply an integral over all space with the exchange-correlation energy density at each point assumed to be the same as in a homogenous electron gas with that density,

$$E_{xc}^{LSDA}[n^\uparrow, n^\downarrow] = \int d^3r n(\mathbf{r})\varepsilon_{xc}^{hom}(n^\uparrow(\mathbf{r}), n^\downarrow(\mathbf{r}))$$
$$= \int d^3r n(\mathbf{r})[\varepsilon_{x}^{hom}(n^\uparrow(\mathbf{r}), n^\downarrow(\mathbf{r})) + \varepsilon_{c}^{hom}(n^\uparrow(\mathbf{r}), n^\downarrow(\mathbf{r}))].$$

(2.32)

For unpolarized systems, the LDA is found simply by setting $n^\uparrow(\mathbf{r}) = n^\downarrow(\mathbf{r}) = n(\mathbf{r})/2$. LDA is best for solids close to a homogeneous gas and worst for very inhomogeneous cases like atoms where the density must go continuously to zero outside the atom. The other approximation is GGA, which is a marked improvement over LDA for many cases. E_{xc} of GGA with a magnitude of the gradient of density $|\nabla n^\sigma|$ is written as

$$E_{xc}^{GGA}[n^\uparrow, n^\downarrow] = \int d^3r n(\mathbf{r})\varepsilon_{xc}(n^\uparrow, n^\downarrow, |\nabla n^\uparrow|, |\nabla n^\downarrow|, \ldots)$$
$$= \int d^3r n(\mathbf{r})\varepsilon_{x}^{hom}(n)F_{xc}(n^\uparrow, n^\downarrow, |\nabla n^\uparrow|, |\nabla n^\downarrow|, \ldots),$$

(2.33)

where F_{xc} is dimensionless and $\varepsilon_{x}^{hom}(n)$ is the exchange energy of the unpolarized gas. Unlike LDA, the spin-scaling relationship should be considered in GGA, and in particular, for $F_x(n, |\nabla n|)$ of the polarized system. As there are numerous forms that F_x may take, many kinds of GGA methods have been proposed so far, such as Becke (B88),[14] Perdew and Wang (PW91),[15,16] and Perdew, Becke, and Enzerhof (PBE).[17]

2.3. The basis set

2.3.1. Plane wave and localized basis function

Modern electronic structure methods can be categorized into two groups, depending on the choice of basis set for the expansion of the valence orbitals, charge densities and potentials: plane-wave methods or localized atomic orbital methods. In particular, in the case of calculations for solid state materials, generally described by periodic boundary condition (PBC), plane wave basis has several advantages: (1) It is easy to change from a real-space representation (where potential energy V is diagonal) via a Fast Fourier Transformation to momentum-space (where kinetic energy T is diagonal). (2) The Hellmann-Feynman forces acting on the atoms and the stresses on the unit cell may be calculated straightforwardly in terms of the expectation value of the Hamiltonian with respect to the ionic coordinates. (3) Basis set superposition errors (BSSE) that should be carefully controlled in calculations based on local atomic orbital basis sets are avoided. On the other hand, a set of local Gaussian basis functions allows fast calculation of exact Hartree-Fock exchange using analytical integration of the Coulomb potential. The treatment of exact exchange is more difficult with a plane wave basis set.

2.3.2. The projectore-augmented wave method

The projector-augmented wave (PAW) method[18,19] was developed to achieve simultaneously both the computational efficiency of the pseudopotential, such a norm-conserving and ultrasoft pseudopotentials, and the accuracy of the full-potential linearized augmented-plane-wave (FLAPW) method. The weak point of pseudopotential calculations appears in the case where the overlap between valence and core electron densities is not completely negligible because of the nonlinearity of the exchange interaction between valence and core electrons. Unlike the pseudopotential method, The PAW method accounts for the nodal features of the valence orbitals and ensures orthogonality between valence and core wavefunctions, i.e., retaining the feature of full wavefunctions. Therefore, compared to the pseudopotential approach, the accuracy of the PAW method is remarkably improved for, especially, magnetic materials, alkali and alkali earth elements, and 3d transition metal elements on the left side of periodic table. Most

of the calculations in this thesis were performed using the PAW method implemented in VASP(Vienna Ab-initio Simulation package).[20-22]

2.4. Scanning tunneling microscopy

2.4.1. Elementary model of scanning tunneling microscopy

Since scanning tunneling microscopy (STM) was invented by G. Binning and H. Rohrer in 1982,[23-25] it has become a hugely powerful tool for measuring topography and other physical properties of solid surfaces with atomic-scale spatial resolution. STM experiments can be performed in a variety of ambient conditions: air, inert gas, ultrahigh vacuum and liquids, including insulating and cryogenic liquids, even electrolytes. Operating temperature ranges from near absolute zero (–273.16 °C) to a few hundred degrees centigrade.

Figure 2.2 shows a schematic diagram of the scanning tunneling microscope. The STM tip can be precisely positioned using a piezodrive, which consists of three mutually perpendicular piezoelectric transducers: x piezo, y piezo, and z piezo. During operation, the tip-sample distance is controlled to within a few angstroms. Thus, the electron wavefunctions in the tip overlap the electron wavefunctions in the sample surface. A bias voltage, applied between the tip and the sample, causes an electrical current to flow. This current flow is a quantum-mechanical phenomenon, referred to as *tunneling*.
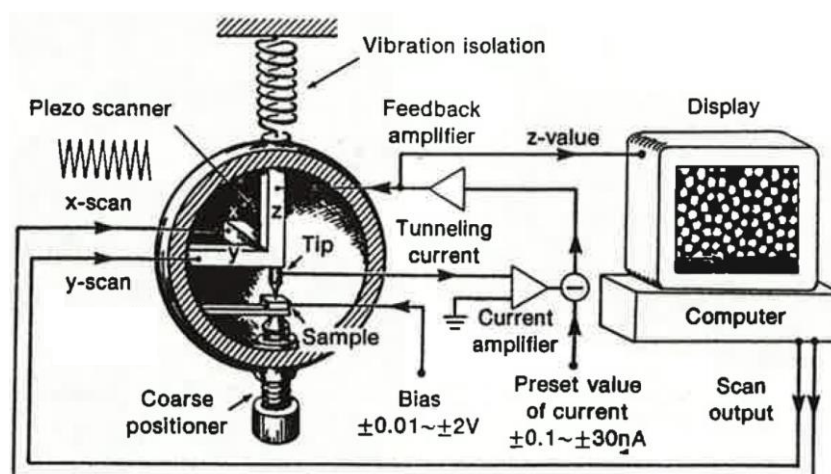

Figure 2.2. Schematic diagram of the scanning tunneling microscope.[Adapted from Reference 4]

19

Figure 2.3 shows a simple model of metal-vacuum-metal tunneling. To simplify the model, the work functions of the tip and the sample are assumed to be same. The work function ϕ of a metal surface is defined as the minimum energy required to remove an electron from the bulk to the vacuum level, taking the vacuum level as the reference point of energy, Fermi energy, $E_F = -\phi$. The tunneling probability w for an electron in the nth sample state to present at the tip surface, $z = W$, is

$$w \propto |\psi_n(0)|^2 e^{-2\frac{\sqrt{2m_e\phi}}{\hbar}W} , \qquad (2.35)$$

where $\psi_n(0)$ is nth sample state, and W is tip-sample distance. By including all the sample states in the energy interval eV, the tunneling current is

$$I \propto \sum_{E_F-eV}^{E_F} |\psi_n(0)|^2 e^{-2\frac{\sqrt{2m_e\phi}}{\hbar}W} . \qquad (2.36)$$

If V is small enough that the density of electronic states does not vary significantly within it, the (2.36) can be conveniently written in terms of the *local density of states* (LDOS) at the Fermi level,
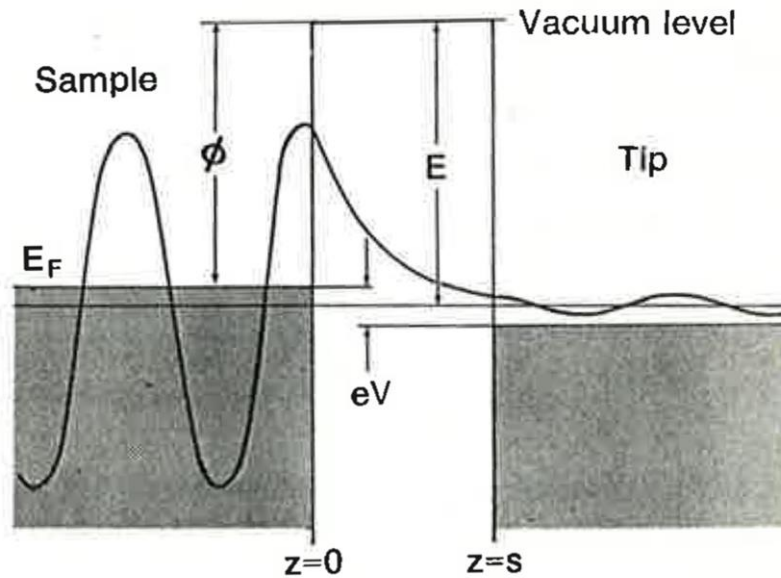

Figure 2.3. Schematic one dimensional metal-vacuum-metal tunneling junction. The sample and the tip are modeled as semi-infinite pieces of free-electron metal. [Adapted from Reference 4]

$$I \propto V \int \rho_S e^{-2\frac{\sqrt{2m_e\phi}}{\hbar}W} . \tag{2.37}$$

Therefore, the number of tunneling electrons, i.e., tunneling current, can be easily tuned by the applied bias and the tip-sample distance. Detailed surface electronic structure, i.e., LDOS, can also be measured with high spatial resolution.

The dependence of the logarithm of the tunneling current with respect to distance is a measure of the work function, or the tunneling barrier height.[26,27] Therefore, from (2.37), the work function of sample can be also measured as

$$\phi = \frac{\hbar^2}{8m_e} \left(\frac{d\ln I}{dW} \right)^2 \tag{2.38}$$

with STM.

2.4.2. Applications of scanning tunneling microscopy

By interrupting the feedback loop, maintaining a constant tip-sample distance while scanning and applying a voltage ramp on the tunneling junction, the tunneling current as a function of bias provides information that is the convolution of the tip DOS and the sample DOS. A detailed description for a scanning tunneling spectroscopy (STS) experiment was suggested by Selloni *et al.*[28] When the temperature is low and the tunneling matrix element is a constant, the tunneling current is a convolution of the tip DOS and the sample DOS over an energy range eV,

$$I \propto \int_0^{eV} \rho_S(E_F - eV + \varepsilon)\rho_T(E_F + \varepsilon)d\varepsilon . \tag{2.39}$$

If the tip DOS is a constant, then (2.39) implies

$$\frac{dI}{dV} \propto \rho_S(E_F - eV + \varepsilon) . \tag{2.40}$$

Therefore, STS is a powerful tool for probing spatial distribution of electronic states of surfaces and adsorbates.

In addition to topographic imaging (STM) and electronic structure measurement (STS), STM can be used to manipulate individual adsorbates.[29] Since D. M. Eigler *et al.* demonstrated the manipulation of Xe atoms on Ni(100) surface using an STM tip in 1989 (Figure 2.4a),[30] numerous later manipulation techniques have been developed using tip-sample interaction, such as pulling, pushing and sliding.[31] As another manipulation technique, vertical manipulation can be enabled by changing the electric field between tip and sample. This involves the transfer of atoms or molecules between tip and surface. For example, the first atomic switch was demonstrated by repeated transfer of Xe atoms between the STM tip and an Ni(100) surface (Figure 2.4b).[32]

Finally, because STM offers tunability of both tunneling current and sample bias, it can be used as an effective electron source for exciting individual molecules. Thus, STM lends itself well to the vibrational spectroscopic method[33-36] for the identification of adsorbate species and the initiation of surface chemical reactions, such as hopping,[37,38] desorption,[38] rotation,[39,40] dehydrogenation[41,42] and dissociation.[43-45] As well, the controllable hopping of a vibrationally excited molecule can be achieved with the aid of a local electric field in an STM junction.[46] Vibrational spectroscopy with STM offers the potential to perform the characterization of single molecules on conductive surfaces. Two methods for accomplishing this have been proposed: inelastic electron tunneling spectroscopy (STM-IETS) and action spectroscopy (STM-AS).[33-36]

STM-IETS, which provides the vibrational spectra (d^2I/dV^2) of single molecules on surfaces, was first demonstrated by Stipe *et al.* in their pioneering study of C_2H_2 on Cu(100) in 1998 (Figure 2.5).[33] Kim *et al.* utilized STM-IETS to identify the chemical specifications of the individual reaction products, inducing the dehydrogenation of a *trans*-2-butene molecule by injecting tunneling electrons. In this experiment, while IET spectrum of *trans*-2-butene showed the signal of C-H stretch mode, both the molecularly deposited 1,3-butadiene and the reaction product showed similar spectral features without the C-H stretch signal, which provided the evidence for the conversion of a *trans*-2-butene molecule into a 1,3-butadiene molecule (Figure 2.6).[41]

STM-IETS is a powerful tool for single molecule vibrational spectroscopy, but STM-IETS can detect only limited kinds of vibrational modes because of its propensity

rule.[47] Also, STM-IETS can be applied to only stable adsorbates against an applied bias. However, many molecules move and react induced by vibrational excitation via inelastic tunneling of electrons. Most motions and reactions cause the tip-surface distance to change, which makes it difficult to carry out STM-IETS measurement. STM-AS is an alternative spectroscopic technology which can be used to measure the vibrational spectra of mobile and reactive molecules in an STM junction.
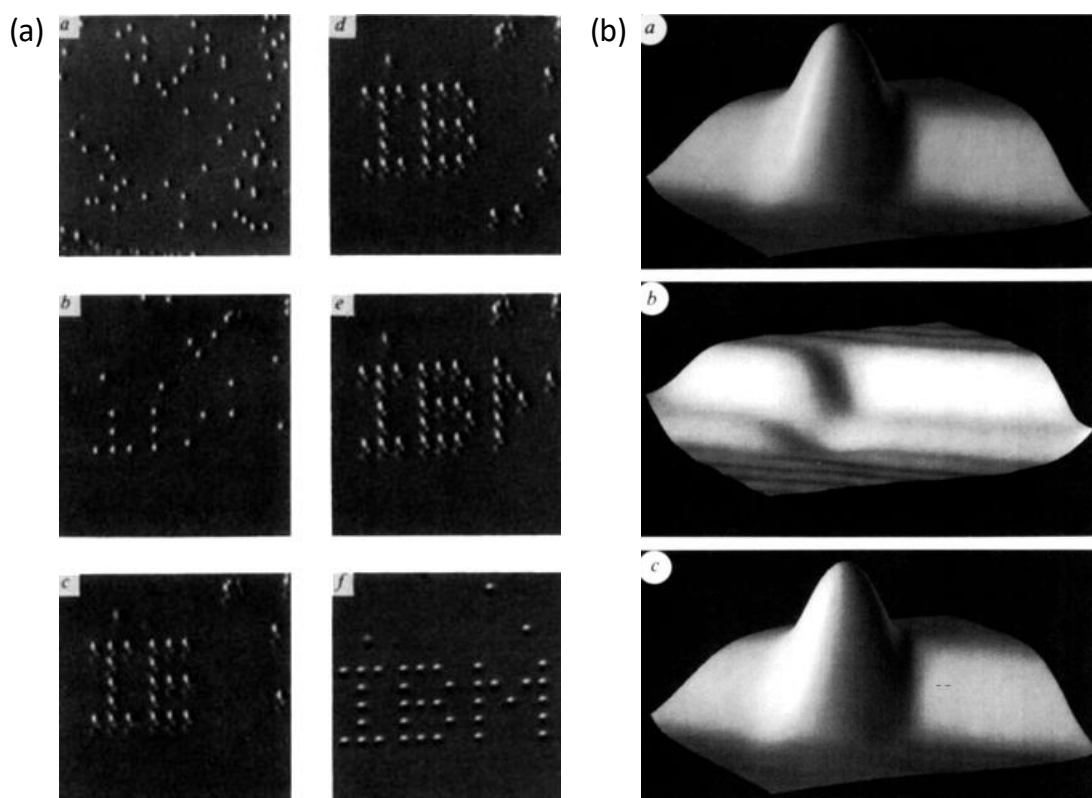

Figure 2.4. (a) Sequential STM images during the construction of a patterned array of Xe atoms on an Ni(100) surface. Each letter is 50 Å from top to bottom [from Reference 40]. **(b)** Sequential STM images (25×25 Å^2) demonstrating the atomic switch involving the transfer of the Xe atom. [Adapted from Reference 42]
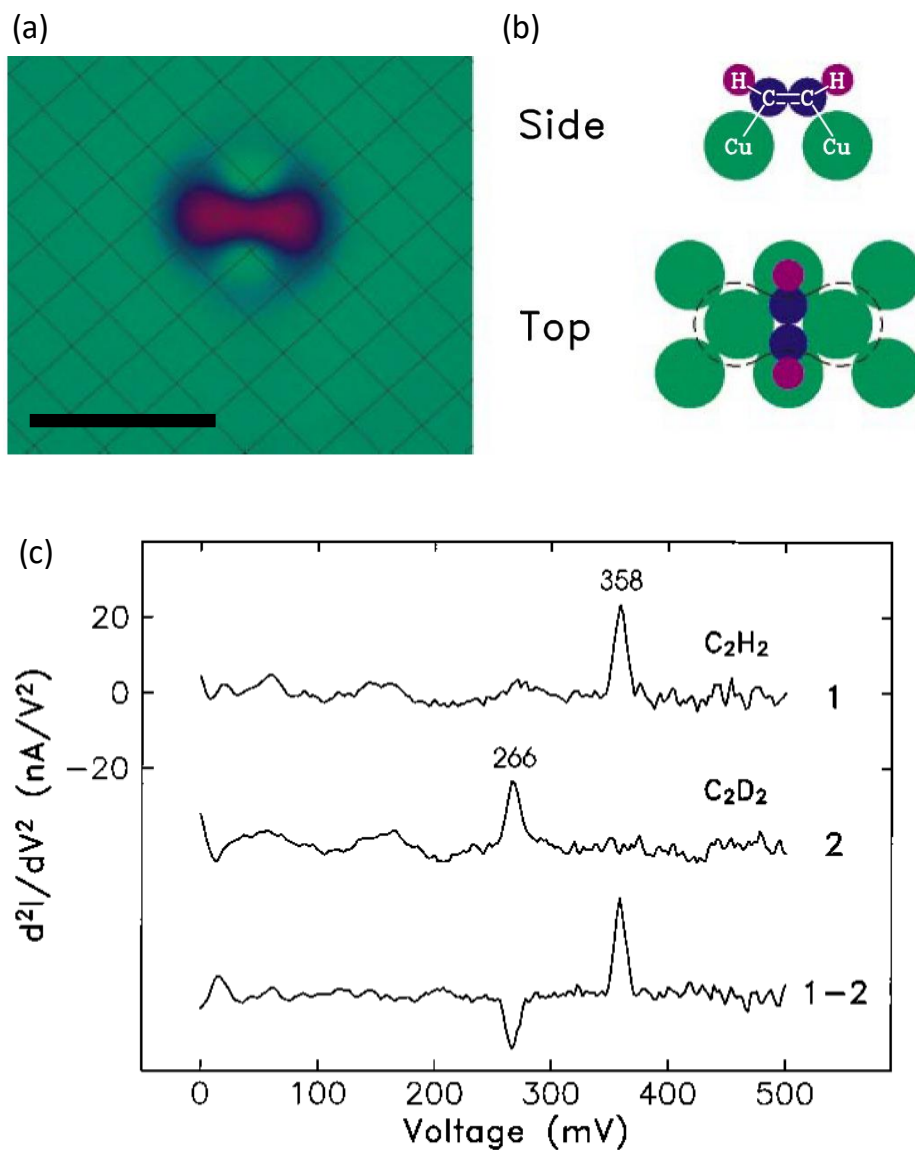
Figure 2.5. (a) STM image of a C_2H_2 molecule on the Cu(100) surface at 8 K (V_s = 100 mV and I_t = 10 nA). Scale bar: 1 nm. (b) Schematic drawing showing side and top views of the molecule's orientation and suggested adsorption site. The dashed line shows the outline of the STM image shape. The dumbbell-shaped depression in STM images may result from π bonding to the Cu atoms perpendicular to the C-C axis, reducing the local density of states for tunneling. (c) STM-IETS spectra for C_2H_2 (1) and C_2D_2 (2) show peaks at 358 mV and 266 mV, respectively. [Adapted from Reference

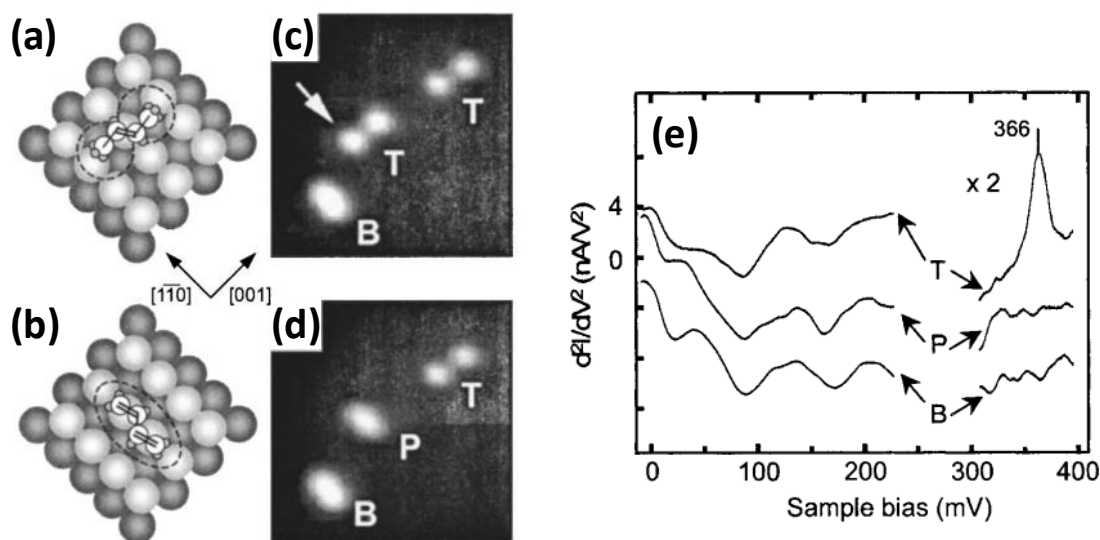**Figure 2.6.** Schematic images of **(a)** *trans*-2-butene and **(b)** 1,3-butadiene adsorbed on Pd(110). STM images showing **(c)** before and **(d)** after inducing dehydrogenation of *trans*-2-butene on Pd(110) at 5 K. **(e)** STM-IET spectra for *trans*-2-butene (T), reaction product (P), and 1,3-butadiene (B). [Adapted from Reference 51]

Sainoo *et al.* introduced a new concept in vibrational spectroscopy with STM called "action spectroscopy" (STM-AS) which utilizes vibrationally induced molecular motion and reactions.[34] They measured the action spectrum to investigate vibrationally-induced configurational change in *cis*-2-butene on Pd(110) against applied bias voltage, revealing the energies of vibrational modes by the onset of motion yield *Y(V)* (Figure 2.7). The first observation of molecular motion induced by vibrational excitation was accomplished by Stipe *et al.*[40] The C_2H_2 molecule rotated when sample bias voltage was higher than the C-H stretch mode energy. The onset energy of the *Y(V)* and the peak in the $\Delta \log Y / \Delta V$-plot were identical to the peak energy in STM-IETS, which indicated that a selective excitation of the C-H stretch mode is a trigger for rotation (Figure 2.8). The power law dependence and sample bias dependence of *N* suggested that direct multiple excitation of the vibrational mode induced the reaction. The bias dependence of *N* was explained by considering that the number of vibrational quanta which can be excited by single electron depends on sample bias while the number of quanta required for the reaction is fixed (Figure 2.9).
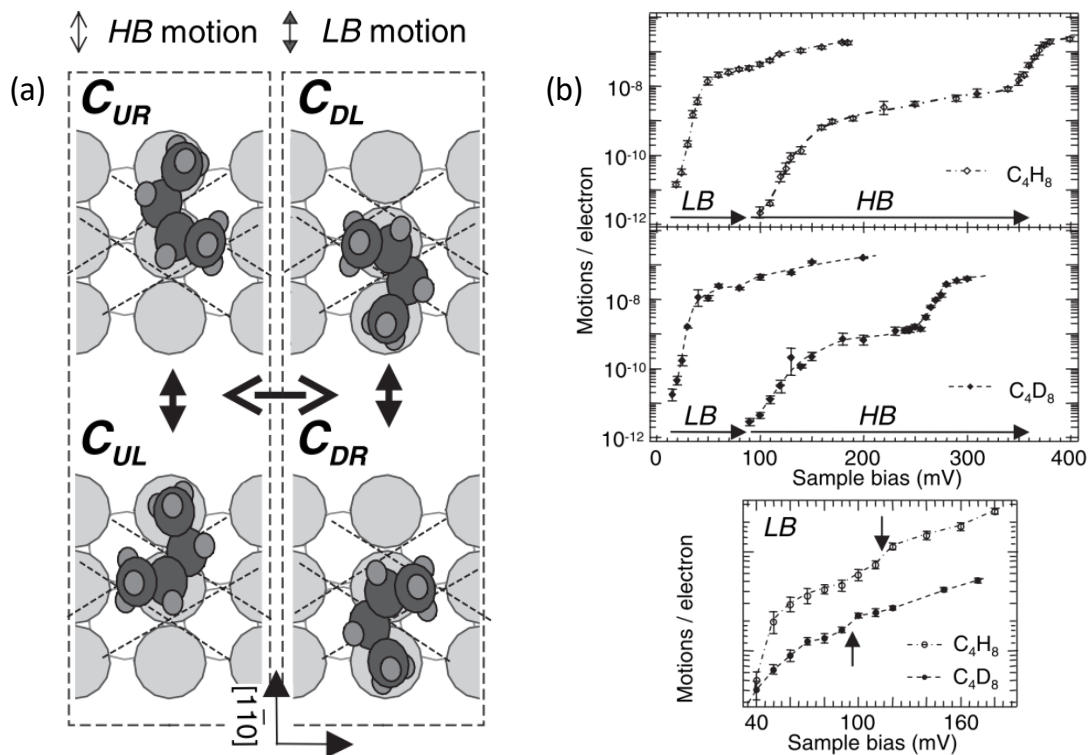
Figure 2.7. (a) Adsorption structures of *cis*-2-butene on Pd(110) at four equivalent adsorption orientations. The suffixes UR, UL, DR, and DL correspond to the relative location of the head part, i.e., up-right, up-left, down-right, and down-left, with respect to the center of the molecule in the STM images (see Figure 1a in Reference 44), respectively. LB and HB denote "low" and "high" barriers, respectively. **(b)** Action spectra for described motions both of C_4H_8 (upper) and of C_4D_8 (middle). Data were taken under fixed tunneling current of 3 nA for C_4H_8 and of 2 nA for C_4D_8. Magnification of the action spectrum for low barrier motion at around the threshold energy (lower). A slight increase in the yield was observed around 115 mV for C_4H_8 and 95 mV for C_4D_8, as indicated by arrows, respectively. [Adapted from Reference 44]

26
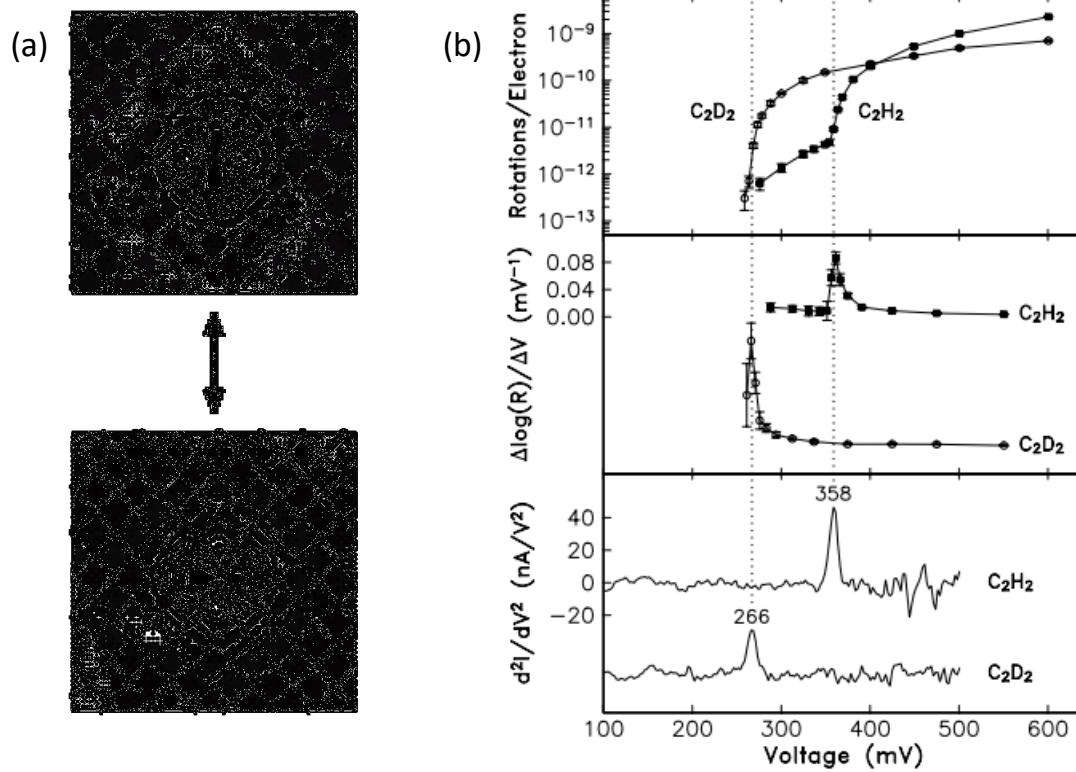
Figure 2.8. (a) STM images of before and after inducing the rotation of C_2H_2 on Pt(111) at 8 K. **(b)** STM-AS, $\Delta \log Y / \Delta V$-plot, and STM-IET spectra of C_2H_2 and C_2D_2 rotation on Pt(111). [Adapted from Reference 50]
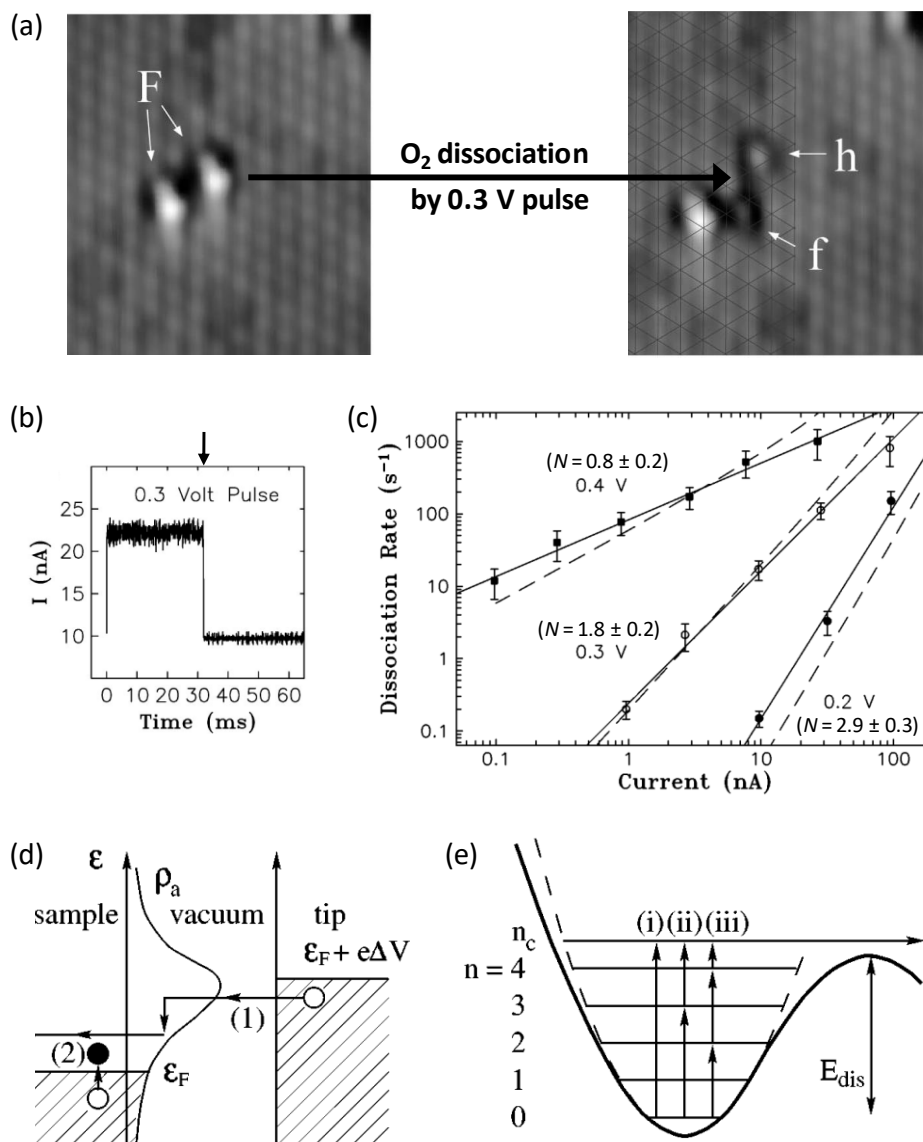
Figure 2.9. (a) STM images of the dissociation of O_2 on Pt(111). **(b)** Current during a 0.3 V pulse over the molecule on the right showing the moment of dissociation. **(c)** Dissociation rate, $R(I)$, as a function of tunneling current, I, for various applied biases. The solid lines are least squares fits to the data and correspond to power laws, $R(I) \sim I^N$. **(d)** Schematic picture of the model for the dissociation of O_2 molecule on Pt(100) by inelastic electron tunneling. **(e)** Schematic picture for the dissociation via multiple vibrational excitation by tunneling electrons; (i), (ii), and (iii) are corresponding to the applied biases, 0.4, 0.3, and 0.2 V, respectively. [Adapted from Reference 53]

28

Detailed explanations for the mechanisms of STM-IETS and STM-AS were fully discussed in the Ph.D. thesis written by K. Motobayashi.[48] It is particularly noteworthy to introduce the theoretical fitting method proposed Motobayashi *et al.*[36,48] for the spectra obtained from STM-AS studies, because it allows the determination of key factors such as (i) vibrational energies (Ω), (ii) barriers along reaction coordinates (RC), and (iv) vibrational broadening (γ) reaction orders (N) without using $R(I)$, (iii) transition rates ($1/\tau_{v,RC}$) for overcoming. The definition of the reaction yield Y as a function of sample bias voltage V, $Y(V)$, and the power law dependence of reaction rate, R, can be described as

$$Y(V) = \frac{R(V)}{I_{tot}(V)/e} \tag{2.41}$$

And

$$R(V) = k \cdot \left(I_{in}(V)/e\right)^N, \tag{2.42}$$

respectively, where I_{tot} (I_{in}) denotes total (inelastic) tunneling current, k is a rate constant at a certain temperature, and N is the reaction order. If a Gaussian function (GF) for the vibrational DOS, $\rho_{ph}(\Omega)$, is adapted to takes into account all the possible sources of broadening (γ) including instrumental, thermal and intrinsic broadening during inelastic tunneling process, $I_{in}(V)$ will be given by integrating the GF twice with respect to V multiplied by inelastic conductance, σ_{in},

$$I_{in}(V) = \sigma_{in} f\left(V, \Omega, \gamma\right), \tag{2.43}$$

where γ is the full width at half maximum of the GF. I_{tot} can then be described as

$$I_{tot}(V) = \sigma_0 V + (\sigma_{el} + \sigma_{in}) f\left(V, \Omega, \gamma\right), \tag{2.44}$$

where σ_{el} (σ_0) is the conductance for the elastic current affected (unaffected) by electron-vibration coupling.[49] Since σ_0 is at least one order of magnitude larger than ($\sigma_{el} + \sigma_{in}$),[50] we can assume $I_{tot}(V) \approx \sigma_0 V$. This leads to

$$Y(V) = K \cdot \frac{f(V,\Omega,\gamma)^N}{V} , \qquad\qquad (2.45)$$

where $K = k \cdot \eta_{in}(\sigma_{in}/e)^{N-1}$ and inelastic tunneling fraction, $\eta_{in} = \sigma_{in}/\sigma_0$.

In experiments, tunnel electrons can excite vibrational modes, even when their energies (Ω_i) are lower than eV, through various multiple excitation channels as shown in Figure 2.10.[48] In that case, first, the excitation of each vibrational mode can independently contribute to a total reaction yield (Figures 2.10a and 2.10b), thus (2.44) can be extended as

$$Y_{tot}(V) = \sum_i K_i \cdot \frac{f(V,\Omega_i,\gamma_i)^{N_i}}{V} . \qquad\qquad (2.46)$$

Second, the reaction can be initiated by the simultaneous excitation of several different vibrational modes (Figures 2.10c and 2.10d). In this case, R should be proportional to the probability of concurrent excitation of these modes, described as the product of the excitation probability of each mode, and (2.45) is expanded as

$$Y_{tot}(V) = \sum_i Y_i(V) = \sum_i K_i \cdot \frac{\prod_j f(V,\Omega_{i,j},\gamma_{i,j})^{n_{i,j}}}{V} , \qquad\qquad (2.47)$$

where j is the index of vibrational modes involved to generate a vibrational peak indexed by i. $n_{i,j}$ is the partial reaction order, the number of electrons required in the multiple excitation of the j mode for the reaction. The conventionally used total reaction order N_i that appears in the power law dependence $R(I) \propto I^N$ is given by

$$N_i = \sum_j n_{i,j} . \qquad\qquad (2.48)$$

Therefore, $Y(V)$ is fully described in terms of vibrational energy, reaction order, rate constant and vibrational broadening, which allows the quantitative analysis of an action spectrum for the motion of single adsorbate. In particular, this method was utilized in determining the vibrational mode of water molecules, which plays as a channel for

their hopping and dissociation motions on ultrathin MgO film grown on Ag(100) support.[45]

        Finally, see also Table 1.4.1 in Reference 58 for a comprehensive list of previously performed studies about vibrationally-mediated motions and reactions of single adsorbates on metal surfaces observed by STM.
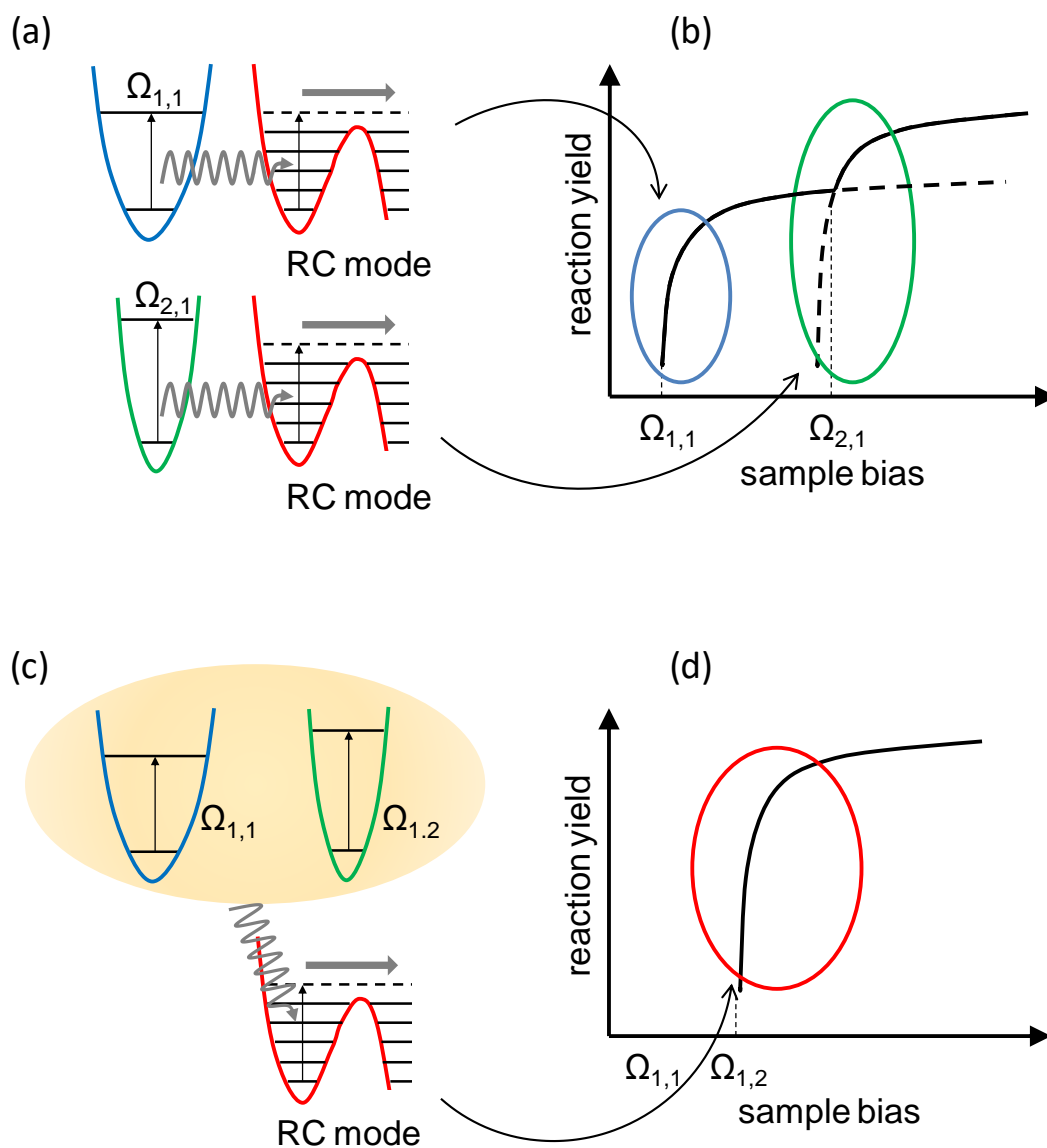
Figure 2.10. Schematic diagrams of the contribution of each mode in multi-mode excitation. **(a)** Two vibrational modes ($\Omega_{1,1}$, $\Omega_{2,1}$) independently contribute to the reaction. **(b)** In the case of (a), two vibrational signals appear. **(c)** Simultaneous excitation of two vibrational modes ($\Omega_{1,1}$, $\Omega_{1,2}$) induce the reaction. **(d)** In the case of (c), only one vibrational signal appears, which corresponds to the vibrational mode with higher energy. At this bias, the lower energy mode also can be excited. [Adapted from

3. Results and Discussion

3.1. Highly-ordered hydroxylation on graphene/Cu(111)

3.1.1. Introduction

Despite the extraordinary physical and electrical properties of graphene, its semi-metallic electrical properties have restricted its use in the wide range of potential applications for this material.[51,52] Numerous efforts have been devoted to achieve a reproducible band gap in graphene based materials.[53-66] One approach involves structural engineering to make a one-dimensional (1D) graphene structure, such as graphene nanoribbons,[53-55] graphene nanowrinkles[56] or a graphene nanomesh[57] for inducing 1D quantum confinement. More conventional and practical approaches are based on chemical modification, i.e., functionalization, on the basal plane of the graphene sheet, for transforming sp2 carbon into sp3 carbon species. Theoretical expectations have suggested an opened band-gap in such (chemically modified) graphene derivatives, and various reactions have been experimentally demonstrated for the chemical modification of graphene, such as hydrogenation,[58-62] oxidation,[63] fluorination,[64,65] and methylation.[66] Nevertheless, most of the results have not reported an opened band-gap as large as that which is predicted in the calculations of idealized structures.[58,59,65,66] This discrepancy between theoretical predictions and experimental observations could originate from the difference between the actual chemical structure and the model structure used in the calculation1.[67,68] While periodic superstructures with highly ordered functional groups are used for the theoretical calculations, the functional groups produced by experiments are typically randomly distributed on the graphene. The development of a new chemical route is therefore needed to facilitate the generation of periodically patterned functional groups on graphene, whose chemical structure is the same as that used for the theoretical calculation. Here, we report the vapor phase hydroxylation reaction on epitaxial graphene on Cu(111), which results in a highly-ordered ($\sqrt{3}\times\sqrt{3}$)R30o superstructure of hydroxyl groups on the graphene surface.

3.1.2. Method

We did a computational study based on periodic density functional theory (DFT) for explaining the well-ordered functionalization of epitaxial graphene (EG) grown on Cu(111), in which the hydroxyl groups from thermal cracking of water vapor were used as a functional group for EG/Cu(111). We used van der Waals density functional (vdW-DF) methodology, i.e., optB86b-vdW functional[69], for taking the vdW interaction into account, which has been successfully applied to describe the interfacial interaction between graphene and metal substrates.[70] All of the calculations were performed using the Vienna Ab-initio Simulation Package (VASP) code.[20,21] The core electrons were replaced by projector-augmented wave (PAW) pseudopotentials,[19] expanded in a basis set of plane waves up to a cutoff energy of 500 eV. The calculated lattice constants are 3.599 Å for Cu, which agrees well with the experimental value,[71] 3.595 Å. We approximated a (1×1)-EG on Cu(111) substrate for simplicity, which resulted in a discrepancy of ~3% for the lattice constant of the graphene on the metal substrates, i.e., 2.545 Å on Cu(111), compared with that of pristine graphene (2.467 Å) at the level of optB86b-vdW. For the relative position of a graphene sheet with respect to the metal substrate which is considered to be the most stable, half of the C atoms are located on top of metal atoms and the other C atoms are located at the fcc hollow site of the (111) metal substrate.[72,73] The $(\sqrt{3} \times \sqrt{3})$R30° and $(3\sqrt{3} \times 3\sqrt{3})$R30° surface supercells were employed for describing the superstructures observed in the experiment and for examining the isolated dimeric interaction between two hydroxyl groups on EG/Cu(111) (Fig. S4), respectively. The slab models consist of a single graphene layer and six copper layers, in which two bottom layers are fixed in their bulk positions. Ionic (electronic) relaxations were performed until atomic forces (energies) were less than 0.01 eV/Å (10–7 eV). The periodically replicated slabs were separated by a vacuum region of ~17 Å. A dipole correction was applied to avoid interactions between the periodic slab images. The k-point sampling of the Brillouin zone was used with 15×15×1 and 5×5×1 Γ-centered grids for the $(\sqrt{3} \times \sqrt{3})$R30° and $(3\sqrt{3} \times 3\sqrt{3})$R30° supercells, respectively. We investigated the detailed electronic structures using the partial charge densities plotted by a VESTA program,[74] and the doping characters of graphene sheet using Bader population analysis.[20]

3.1.3. Experimental observation: highly-ordered OH adsorption

The gas phase hydroxylation was carried out by exposure of the EG sample to thermally cracked H_2O vapor (vapor exposure of 30 Langmuir), and thereby atomic hydrogen and -OH groups only are introduced on graphene, without other typical functional groups, in contrast to the conventional oxidation process for producing graphene oxide that yields many epoxide groups.
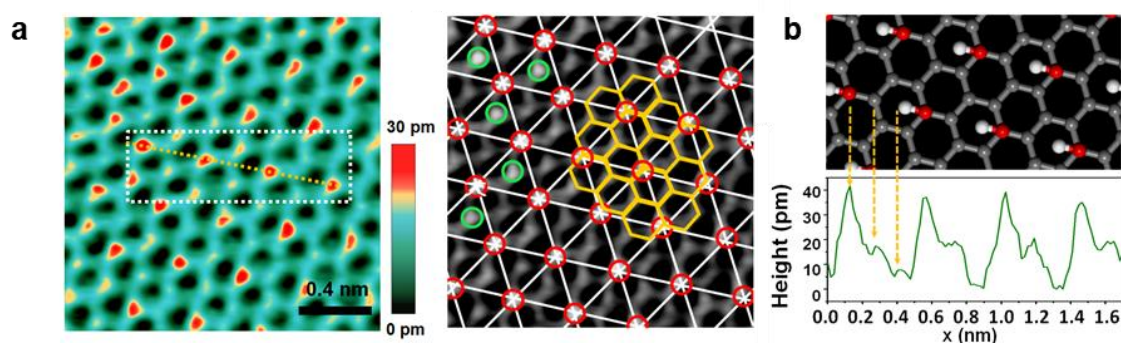

Figure 3.1. (a) High-resolution STM images of EG-OH surface by a molecule-modified STM tip

(b) The predicted atomic configuration and height profile

The higher resolution STM image (Fig. 3.1(a)) obtained by the molecule-modified tip visualizes the exact bonding site of the functional group, which is not at a bridge site but is on top of the carbon atom. Therefore, we identify that the -OH group is the main functional group resulting from the functionalization of EG by the thermal cracking of H2O vapor, because an ether group would be observed at a bridge site.[63] The proposed model structure (EG-OH) is on Fig. 3.1(b). A height profile along the orange-dotted line shows the obvious height difference between the functional groups on top of the carbon atoms ($\sim$40 pm) and the unreacted carbon atoms ($\sim$15 pm). Our data support the formation of -OH groups rather than epoxide groups, which is probably due to the higher population of $\cdot$OH radicals compared to that of atomic oxygen in cracked H_2O vapor. We note that the OH preferentially adsorb on red circle position in Fig. 3.1(a), which is identified as $C_6(OH)_1$ [hereafter, $C_6(OH)_1$ denotes the superstructure of an EG with $C_6(OH)_1$ stoichiometry] with P6m space group, and second favorable adsorption is green circle position in Fig. 3.1(a) with higher coverage ($C_6(OH)_2$) , whose space group is P3m1.

3.1.4. DFT calculation and the electronic band structure of EG-OH

In order to further understand the formation of $C_6(OH)_1$ and its electronic structure, periodic density functional theory (DFT) calculations were carried out using van der Waals density functional (vdW-DF) methodology and a plane wave basis set. The optimized geometries of EG, $C_6(OH)_1$, and $C_6(OH)_2$ that were observed by STM, are presented in Fig. 3.2-i to Fig.3.2-iii. Because the two carbon atoms at the meta-positions (marked with yellow circles in Fig. 3.2-ii) with respect to the hydroxyl groups remain unbonded in the unit cell of $C_6(OH)_1$, we extended our computational study by studying the fully functionalized superstructure, i.e., $C_6(OH)_3$, despite its absence in our experimental observations (Fig. 3.2-iv). The hydroxylation in the manner of bonding at the meta positions with respect to the other -OH group can be understood in terms of the favorable interfacial interaction between EG and Cu as a result of functionalization. The formation of a C-OH σ bonding induces sp^3 character not only to the carbon atom bonding with -OH but also to its neighboring carbon atoms which may, therefore, interact more strongly with the Cu atoms beneath them.[75] These C-Cu distances are 2.18, 2.07, and 2.01 Å for $C_6(OH)_1$, $C_6(OH)_2$, and $C_6(OH)_3$, respectively, which are significantly shorter than the interfacial C-Cu distance (3.18 Å) of EG/Cu(111) before functionalization (Fig. 3.2).
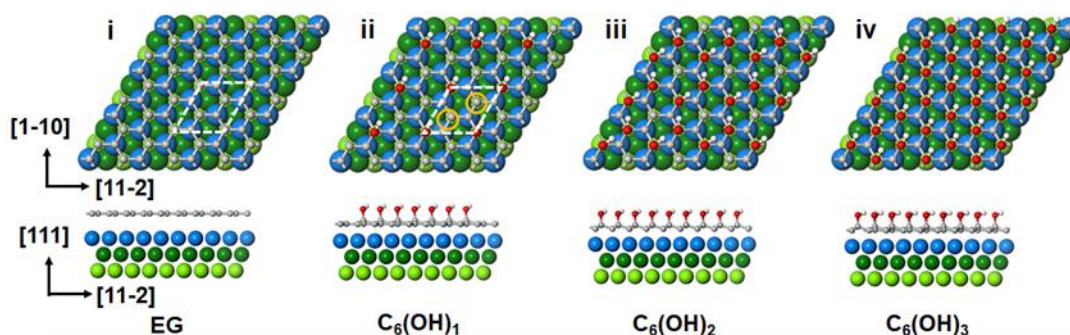
Figure 3.2. The optimized atomic geometries for EG, $C_6(OH)_1$, $C_6(OH)_2$ and $C_6(OH)_3$ [first, second and third Cu layers: blue, dark green and light green spheres, respectively]. The $(\sqrt{3}\times\sqrt{3})R30°$ unit cell employed in the periodic DFT calculations is denoted with a white parallelogram.

The estimated relative stabilities for the adsorption structures of two -OH groups isolated from the other functional groups also indicate that the meta position with respect to the first -OH is the most likely bonding position of the second -OH group (Fig. 3.3).

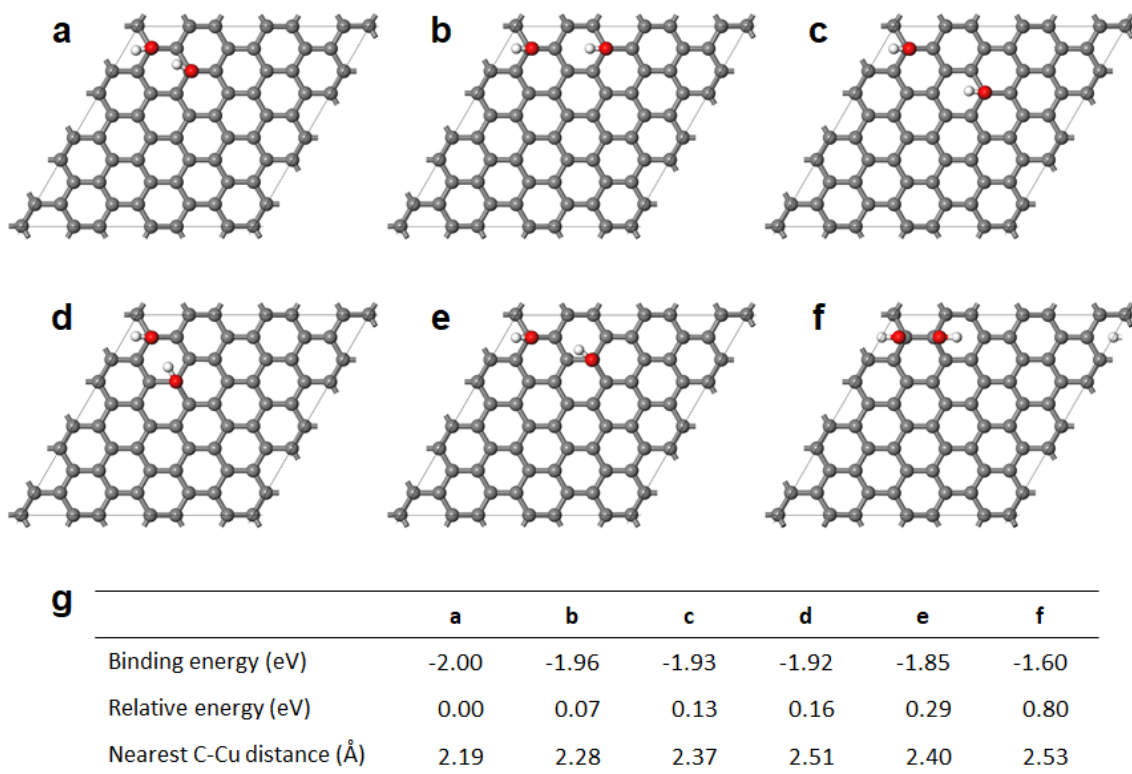| g	a	b	c	d	e	f
Binding energy (eV)	-2.00	-1.96	-1.93	-1.92	-1.85	-1.60
Relative energy (eV)	0.00	0.07	0.13	0.16	0.29	0.80
Nearest C-Cu distance (Å)	2.19	2.28	2.37	2.51	2.40	2.53

Figure 3.3 (a-f) The optimized atomic geometries for six dimeric configurations. To investigate the isolated dimeric interactions, a $(3\sqrt{3} \times 3\sqrt{3})R30°$ unit cell was employed in periodic DFT calculations. The copper layers are omitted for clarity. (g) The binding energy per one OH (Eb/OH, eV), the relative energy (eV), and the nearest C-Cu distance (Å) for the six dimeric configurations. The binding energy per one OH (Eb/OH) is calculated as $E_b/OH = E(n\text{OH-EG/Cu(111)}) - [nE(OH) + E(\text{Gr/Cu(111)})] / n$, $n = 2$

The computationally evaluated binding energies per one -OH group (E_b/OH) in the unit cell of EG/Cu(111) are –2.23, –2.19, and –1.98 eV for $C_6(OH)_1$, $C_6(OH)_2$, and $C_6(OH)_3$, respectively. The computational results show that E_b/OH decreases as the number of -OH groups in the unit cell increases. Considering the sequential binding of an -OH group to EG, i.e., $C_6(OH)_1 \rightarrow C_6(OH)_2 \rightarrow C_6(OH)_3$, the calculated E_b of the second and third -OH are smaller than that of first -OH by 0.09 and 0.67 eV, respectively. The significant decrease in E_b for the third hydroxylation can, therefore, reasonably explain our not observing $C_6(OH)_3$. Because our DFT approach is performed using the (1×1)-EG/Cu(111), the instability of the second and third hydroxylation compared to the first hydroxylation is also expected to be larger than the computationally estimated values.

37

The estimated E_b/OH for the superstructures supports the experimental observation of $C_6(OH)_1$ and $C_6(OH)_2$; but $C_6(OH)_2$ might be expected to be close to as prevalent if not more so than $C_6(OH)_1$ given the small difference (0.04 eV) between the E_b/OH of $C_6(OH)_1$ and $C_6(OH)_2$. Indeed, the adsorption structure of two -OH groups corresponding for $C_6(OH)_1$ is slightly less stable than that for $C_6(OH)_2$ by 0.07 eV when the influence from the other functional groups on the adsorption structure is excluded (Fig. 3.3). The electronic structure, i.e., the local density of states (LDOS), of the -OH groups on EG/Cu can rationalize the overall instability of the OH groups in $C_6(OH)_2$ compared to $C_6(OH)_1$ (Fig. 3.4). Whereas the highest prominent feature in the occupied energy region for the LDOS of the -OH group in $C_6(OH)_1$ is distributed around –2.5 eV with respect to the Fermi level (EF), that in $C_6(OH)_2$ (and also for $C_6(OH)_3$) is located at around –1.2 (–0.8) eV. The deeper energy range for the electronic states of the -OH group with respect to the E_F in $C_6(OH)_1$ indicates its higher stability compared to those in other superstructures.

The change of electronic structure by hydroxylation was investigated with scanning tunneling spectroscopy (STS) measurements (Fig. 3.5a). In a dI/dV spectrum of the Cu(111) surface (black), the surface state of Cu(111) was observed near the sample bias of 0 V.[76,77] In a dI/dV spectrum of EG/Cu(111) (red), the broad band marked by the dotted circle at –1.5 to –0.5 V is considered to originate from the graphene-Cu(111) interaction, and the deep located at –0.8 V marked by a red arrow in the dI/dV curve can be assigned as the Dirac point of graphene according to the previous report of Gao, et al.[78] After hydroxylation (blue), the Dirac point disappears and the band marked by dotted circle is upshifted due to a p-doping effect by hydroxyl groups. Bader population analysis also indicates the change in doping character of graphene sheet due to hydroxylation, in which the partial charge of graphene sheet in unit cell of EG/Cu(111) and $C_6(OH)_1$ are –0.04e (n-doped) and +0.12e (p-doped), respectively. New electronic states appear at -2 to ~ -1 V, which would originate from destruction of the π conjugation network due to the formation of the sp^3 C-OH bonds, in dI/dV spectrum of EG-OH/Cu(111). The influence of hydroxylation on the electronic structure of EG/Cu(111) was further investigated with a band diagram analysis as shown in Fig. 3.5b. It is well known that a metallic substrate can alter the electronic structure of graphene.[72,73] Due to charge transfer from Cu to EG, the n-type doped character of graphene is indicated by the conical point of the Dirac cone located at the –0.45 eV with respect to the E_F (Fig. 3.6a). The electronic structure of EG/Cu(111) is significantly modified by functionalization with -OH groups on its basal plane. The conical dispersive curves at EG/Cu(111) split into three states due to the

interfacial interaction, i.e., Cu d_{z^2} - C p_z interaction (see also Fig. 3.4), induced by hydroxylation. The band energy for the π states of the unbonded carbon atoms located at the meta position with respect to the -OH group is –0.25 eV from the EF at the Γ point. Two π states of the neighboring carbon atoms from the carbon atom bonding with the OH group interact with the Cu d_{z^2} states (see the partial charge density plots in Fig. 3.5b), and their band energies are –0.04 and 0.02 eV from the EF at the Γ point. The band diagram for $C_6(OH)_1$ thus shows a band gap opening of 0.21 eV. The characteristic features of the Dirac cone are significantly destroyed by further functionalization of EG/Cu(111), i.e., $C_6(OH)_2$ and $C_6(OH)_3$ (see Fig. 3.6).
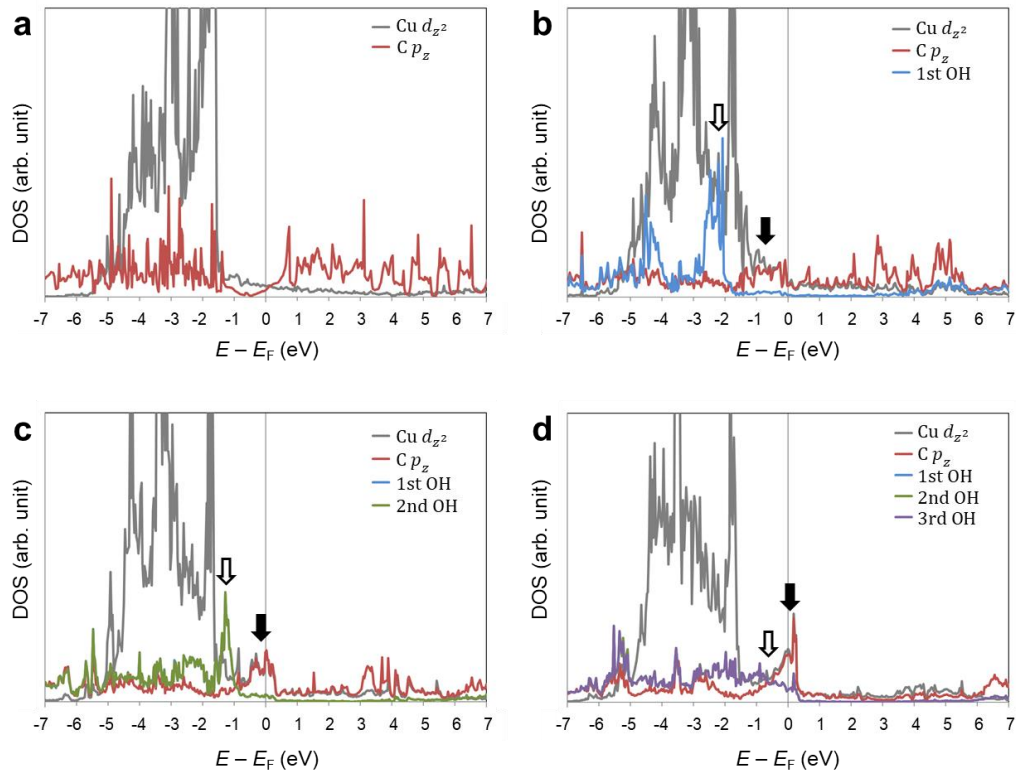
Figure 3.4 Projected density of states (PDOS) for the d_{z^2} state of the Cu substrate and the p_z state of epitaxial graphene (EG), and the local density of states (LDOS) for the hydroxyl functional group on EG: (a) EG/Cu(111), (b) $C_6(OH)_1$, (c) $C_6(OH)_2$, and (d) $C_6(OH)_3$ superstructures. The prominent features of interfacial interaction between the Cu substrate and π states of EG, i.e., the Cu d_{z^2}– C p_z interaction near the Fermi level (EF) are indicated with filled arrows, and the LDOS positions near the EF of the hydroxyl group binding to EG are indicated with unfilled arrows.
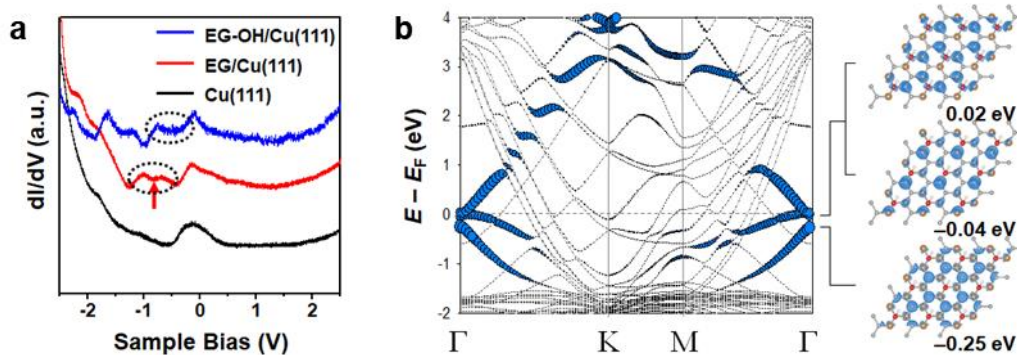
Figure 3.5 (a) dI/dV spectra measured on Cu(111), EG/Cu(111) and EG-OH/Cu(111). The broad band marked by dotted circles indicate the band originated by graphene-Cu(111) interaction. The Dirac point in EG/Cu(111) is marked with a red arrow. (b) Band diagram for C6(OH)1 and the partial charge densities near the Dirac point (at Γ). The relative amount of C 2pz character is proportional to the size of blue dots.
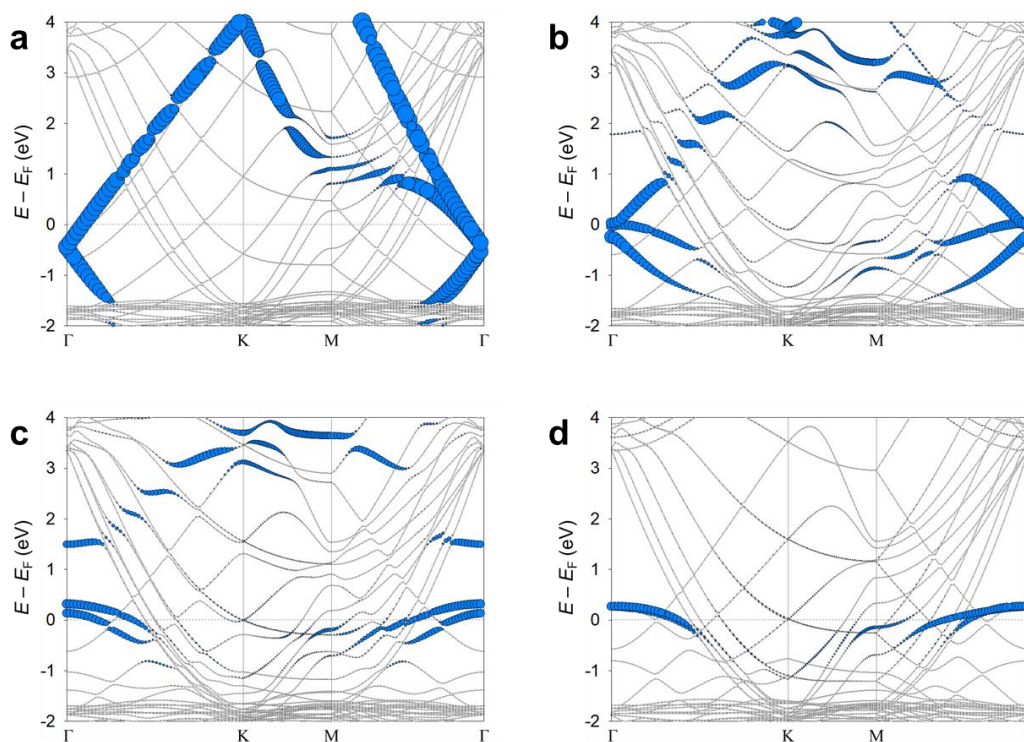
Figure 3.6 Band diagram for (a) epitaxial graphene on Cu(111), EG/Cu(111), (b) $C_6(OH)_1$, (c) $C_6(OH)_2$, and (d) $C_6(OH)_3$ superstructures. The relative amount of C $2p_z$ character is proportional to the size of the blue dots.

40

3.1.5. Conclusion

We studied the vapor-phase hydroxylation of epitaxial graphene both on Cu(111) single crystal samples and on Cu(111) single crystal foil samples and discovered a periodic functionalization with stoichiometry $C_6(OH)_1$. Atomic scale STM combined with spectroscopic studies shows a $(\sqrt{3}\times\sqrt{3})R30°$ superstructure of $C_6(OH)_1$. Theoretical calculations suggest that induced C-Cu 'back bonding' thermodynamically stabilizes the Gr-OH superstructure, and explains the electronic band structure of the EG-OH.

3.2. Electron-induced O₂ dissociation on Ag(110)

3.2.1. Introduction

Adsorption and dissociation of an oxygen molecule are of great interest due to the first step of an oxidation reaction. In industry, the oxidation reaction has been applied for various reactions such as epoxidation of ethylene.[79,80] In particular, investigation on Ag(110) surface is studied intensively because it is the most reactive surface among the low-Miller-index surface for dissociation of O_2 molecule. The chemical reaction of chemisorbed O_2 on Ag(110) was investigated by STM. Three adsorbed states were discovered in early studies (the 80s'-90s') which are the physiosorbed state (< 40 K), two chemisorbed states (40-150 K) and dissociative chemisorbed state (> 150 K). Two chemisorbed states were found, $O_2[001]$ and $O_2[\bar{1}10]$, along with the two directions of the Ag(110) surface with a 90-degree difference. Chemisorption energy of both states are similar as 0.55 eV for $O_2[001]$ and 0.51 eV for $O_2[\bar{1}10]$[81] or same 0.37 eV for $O_2[001]$ and $O_2[\bar{1}10]$[82] in computational results.

Although the adsorption and dissociation reaction of chemisorbed O_2 on the Ag(110) surface has been studied both experimentally and theoretically in the past, the dissociation mechanism is still a controversial issue. STM experimental studies reported four-fold hollow site is thermodynamically favored for both O_2 molecule.[81-93] J. R. Hahn et al., studied reaction path and threshold energy for dissociation. Dissociation of $O_2[\bar{1}10]$ along the same direction is 480 meV whereas there is a bias dependency for $O_2[001]$ dissociation. When a negative bias is applied, 85% of $O_2[001]$ underwent dissociation as the same direction at threshold energy of 390 meV and 15% of the molecules 90-degree rotated and dissociated along $[\bar{1}10]$ direction.[88] On the other hand, dissociation under the positive bias happened through $[\bar{1}10]$ direction upper the 470 meV. Rotation only occurred from $O_2[001]$ to $O_2[\bar{1}10]$ and theoretical study calculate the energy barrier between two chemisorbed states is 0.45 eV.[82] Furthermore, molecular beam experiments show that the molecular adsorption of O_2 onto Ag(110) is an activated process. This result indicates that the chemisorbed state is a precursor for dissociation.[94] Despite a large number of previous studies until recently using molecular beam[94-97], no direct dissociation

was found to take place below the incidence energy of 0.9 eV (0.6 eV including the vibrational zero-point energy), even if the minimum energy barrier of dissociation is 0.36 eV which is calculated by DFT calculation.[92] To clearly understand the driving force of reaction, it is important to elucidate the reaction mechanism and pathway of chemisorbed O_2 molecules.

Herein, we first suggest that the mechanism of electron-induced dissociation reaction related vibrationally excited state for both $O_2[001]$ and $O_2[\bar{1}10]$ molecule on Ag(110) surface. For mechanism study, we investigate the physical property of adsorbate and chemical reaction of the reactant on a surface using scanning tunneling microscopy (STM) at 5.0 K under the ultrahigh vacuum ($< 6.0 \times 10^{-11}$) condition. Oxygen molecules are deposited when the surface temperature is 93 K and the ratio of two O_2 species is almost equal. Inelastic electron tunneling spectroscopy (IETS) results demonstrated that two O_2 molecule states have a different vibration energy value of O-O stretch mode, and which also present at action spectra (AS). All possible paths of reactions are considered and the thresh-old energy was carefully confirmed. The dissociation mechanism of O_2 molecule adsorbed on Ag(110) surface is induced by vibrational excitations of the overtone of the (O-O) stretch mode.

3.2.2. Method

The Ag(110) single crystalline metal substrates were cleaned using repeated cleaning cycles with Ar^+-ion sputtering and annealing around 480 °C in preparation chamber. The surface temperature was 93 K when we deposited the O_2 molecule. The CO molecule was co-adsorbed after O_2 molecule deposition. All experiments were investigated with a low temperature STM (Omicron GmbH) maintained at 5 K under ultra-high vacuum ($< 6.0 \times 10^{-11}$ Torr). The scanning conditions for STM images were V (sample bias-voltage) = 20 mV and I (tunneling current) = 0.1 nA and O_2 molecule for dissociation was selected as solely separated singing molecule avoiding from tip approaching region. The current trace was measured when the STM tip positioned on the

out of center of O_2 molecule at a fixed gap resistance (V = 20 mV, I = 0.1-30 nA). The IETS-STM results were obtained from subtraction surface signal form molecule on surface signal. All results were averaged using 11 IETS data. Total 547 O_2 molecules used for AS spectra.

3.2.3. Electron-induced chemical reaction of O_2 on metal surface

Figure 1. describes the common reaction for the O_2 molecule. There is no bias dependency for all reactions. To distinguish and compare the STM images of two chemisorbed O_2 molecule state and its reaction process, four molecules were used for example. Experimental results are shown in Figure 4.1(a) to (d) and model systems for each STM images are Figure 1. (e) to (h). Rotation from O_2[001] to O_2[$\bar{1}$10] is obviously shown in Fig. 4.1(a) to (b) and threshold energy of this rotation was -200 mV (+280 mV) with 25 nA for a negative (positive) pulse. The opposite direction of rotation from O_2[$\bar{1}$10] to O_2[001] was barely detected but still, exist which is appeared in Fig. 4.2. Most O_2[001] dissociate and O atoms position on four-fold hollow site (FFH) and short bridge (SB) site one each. The O_2[$\bar{1}$10] dissociate along the [$\bar{1}$10] direction and two O atoms are adsorbed on the FFH site. We also examined a threshold energy for dissociation and found that -200 mV with 30 nA (+280 mV with 25 nA) for O_2[001] molecule and 260 mV with 30 nA (+280 mV with 40 nA) for O_2[$\bar{1}$10] molecule which is lower than previous studies. This is the reason why former studies had different O_2[001] dissociation for hot electron and hot hole. In Fig 4.3., the ratio of molecular motion for two chemisorbed O_2 states in 5 days experiments were investigated. For O_2[001] molecules, the rotation was preferred in high positive bias leading the dissociation along the [$\bar{1}$10] direction while only 15% rotation occurred under -390 mV condition which is the same result in previous studies.[88]

Before we discuss the detail of the dissociation mechanism, physical property for an adsorbed molecule on the surface was analyzed. Vibration energy for O_2[001] was already discovered as 85 mV from electron energy loss spectroscopy (EELS)[98], 82 mV from STM-IETS[86] in former studies. In this paper, we also measured vibrational energy

by IETS that can detect the energy of vibration modes in a single molecular level. To clarify the energy of O-O stretch mode, we co-adsorbed the CO molecule with O_2 molecule (Figure 4.4(a)) and compared as a reference. Hindered rotation mode of CO was confirmed at ±19.5 mV which is well-matched with the value from the previous study, ±18.5 mV.[99] In peak at ±78.8 mV for $O_2[001]$ in Figure 4.4(c) is assigned to the O-O stretch mode, in a good agreement with EELS results. Vibrational spectra of $O_2[\bar{1}10]$ was also studied, however, there was no data because of the lack of IETS signal.[100,101] By repeated measurement, we observe peak at ±87.2 mV after the smoothing row data even signal-to-ratio is high. It is worth that this is the first report for analysis of vibration mode for $O_2[\bar{1}10]$ in an experiment.
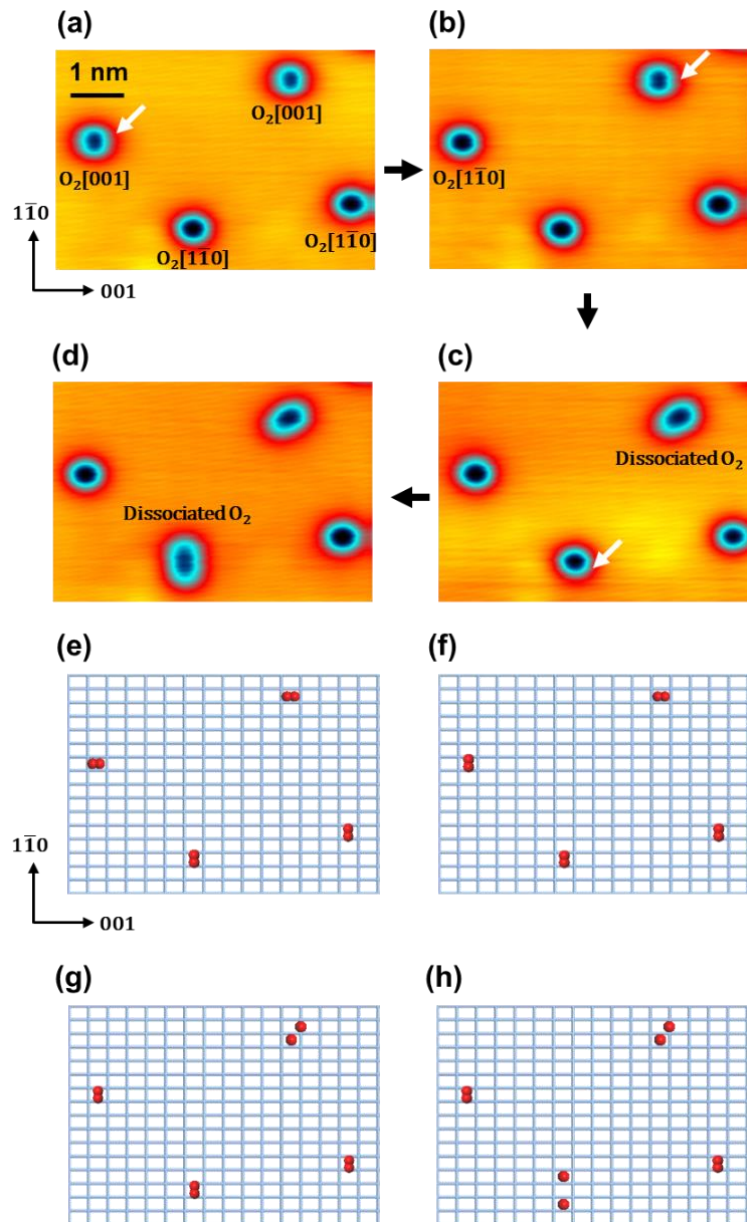
Figure 4.1. Rotation and dissociation of O_2 molecule on Ag(110). There are two chemisorbed O_2 molecule on hollow site aligned along the [001] and [$\bar{1}10$] direction of Ag(110). Reaction happens on molecule which pointed by white arrow. (a) Two O_2[001] and two O_2[$\bar{1}10$] molecules adsorbed on Ag(110) (b) Rotation reaction from O_2[$\bar{1}10$] to O_2[$\bar{1}10$]. (c) Dissociation reaction of O_2[001]. Two O atoms are positioned at hollow site and bridge site, respectively. (d) Dissociation reaction of O_2[$\bar{1}10$]. Two O atoms are positioned at hollow sites. Dissociation occurs in the original direction of O_2 molecule. STM images obtained by bare W tip at voltage of 20 mV and a tunneling current of 0.1 nA. (e)-(h) are model description for (a)-(d) STM images.

46

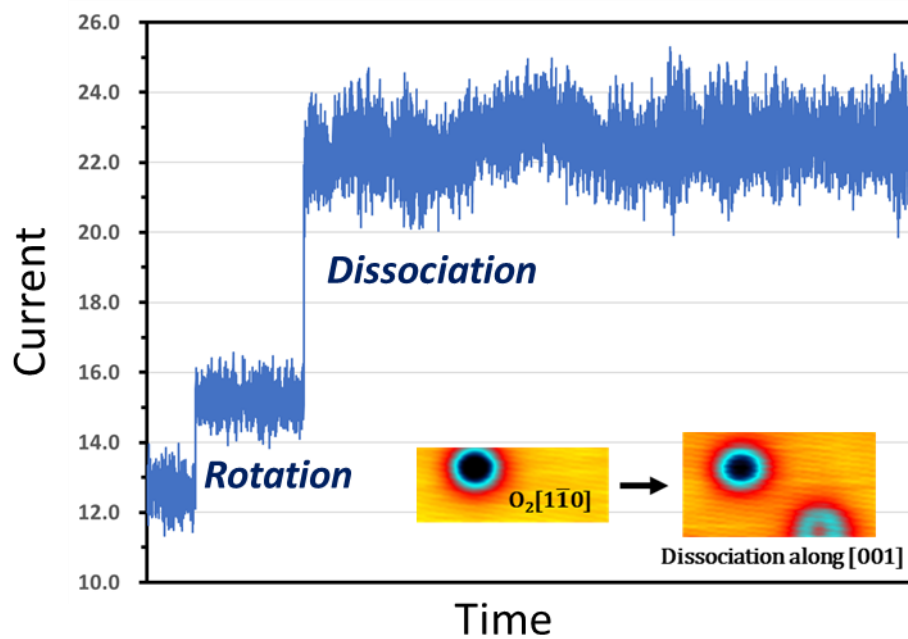**Figure 4.2.** Current trace for rotation and dissociation of $O_2[\bar{1}10]$ molecule on Ag(110). The $O_2[\bar{1}10]$ molecule dissociate along [001] direction via two reaction step, which were rotation and dissociation.
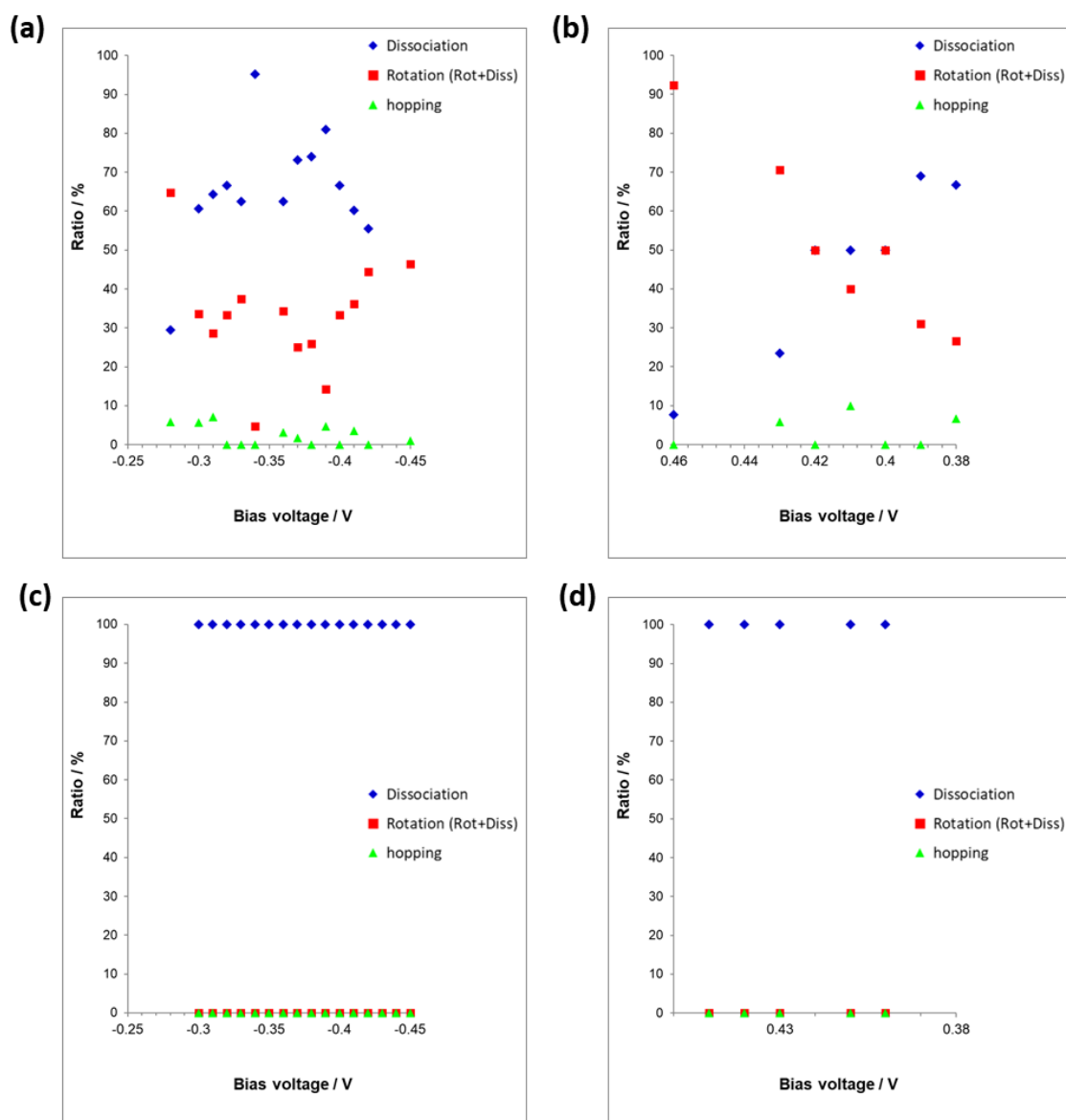
Figure 4.3. Summary of detected reactions for 5 days. (a) and (b) is on $O_2[001]$ molecules. (c) and (d) is on $O_2[\bar{1}10]$ molecules.
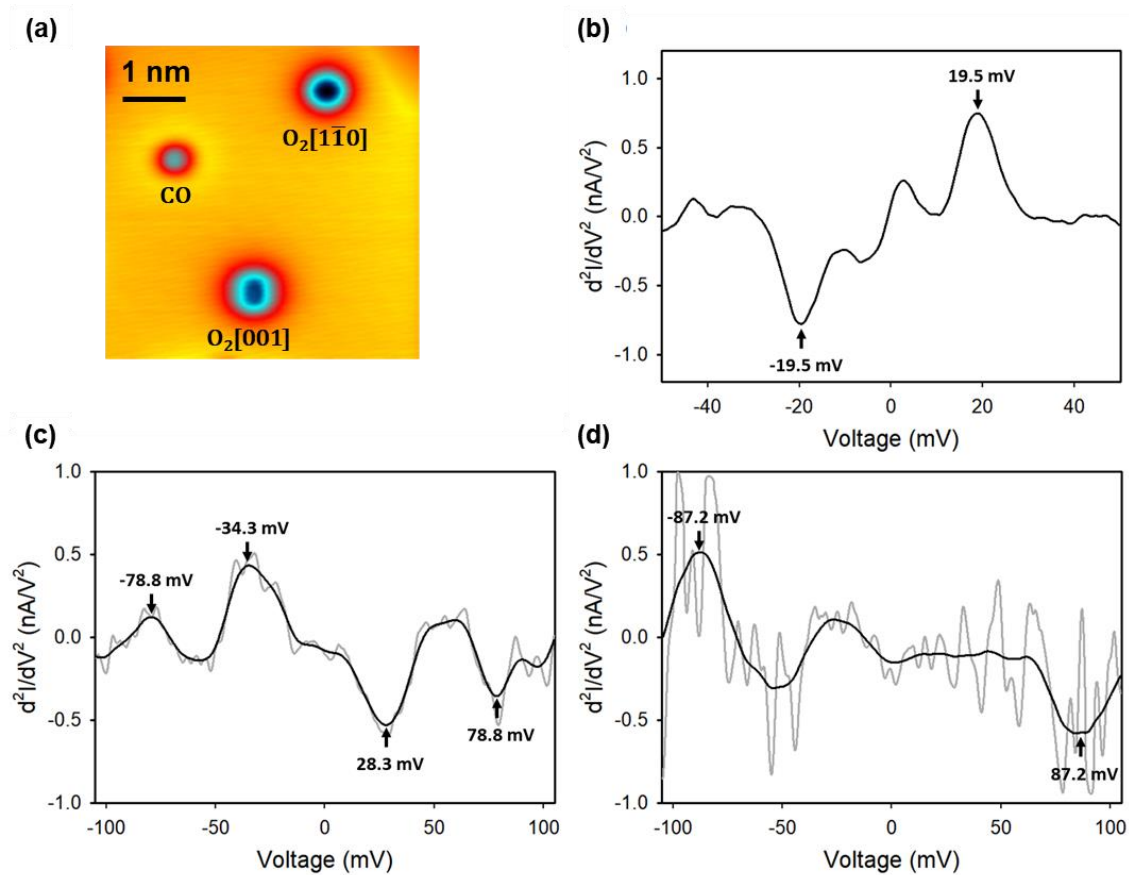
Figure 4.4. STM image of CO molecule and O_2 molecules co-adsorption. STM-IETS for (b) CO, (c)O_2[001] and (d) O_2[1-10] molecule on Ag(110). The spectra are average of multiple scans from -50 mV to 50 mV, from -105mV to 105 mV for CO and O_2 molecules, respectively.

We interpreted the action spectrum with scanning tunneling microscopy (STM-AS) for chemisorbed O_2 molecule. STM-AS informs about the relationship between specific vibration mode and reaction from the value when yield Y(V) hopping at a certain voltage which corresponding the multiples of vibration mode energy. The Y(V) The chemisorbed O_2 molecule has a low density of states (DOS) on unoccupied states, which means molecular orbitals (MOs) of O_2 is almost filled with electrons.[101] In other words, injecting the hot electron under a positive bias is particularly difficult than injecting the hot hole under negative bias. This is reflected in STM-AS results (Fig.4.5), AS for a positive bias shows 2-order lower reaction yield having the same Y(V) voltage then negative bias. We represent AS on negative bias for both $O_2[001]$ and $O_2[\bar{1}10]$ molecules. Spectral fitting of the STM-AS spectra was conducted to drive additional data about the dissociation of O_2 molecule and detailed fitting information explained in ref 48 and ref 58. The Y(V) handling the multi-electron process can be defined as

$$Y(V) = K_{eff} \; \frac{F(V, \hbar\Omega, \sigma_{ph})^n}{V}, \tag{1}$$

where K_{eff}, $\hbar\Omega$, σ_{ph} and n indicate the effective prefactor, the vibrational energy responsible for the equation, the vibrational broadening factor, and the reaction order, respectively. In this formula, F (V, $\hbar\Omega$, σ_{ph}) can be derived by integrating twice the effective vibrational DOS expressed with Lorentzian function.[43,102] There are clear Y(V) hopping at -294 mV and -367 mV for $O_2[001]$ which expected as vibrationally excited energy of O-O stretch mode from $v = 0$ state to $v = 4$ and 5 state, respectively. To figure out the vibration energy of O-O stretch mode and anharmonicity constant, fitting the value from IETS and AS by Morse potential energy which is written approximately in Eq (2):

$$Ev = \hbar\omega_e \left(v + \frac{1}{2}\right) - \hbar\omega_e\chi_e \left(v + \frac{1}{2}\right)^2, \tag{2}$$

where v, $\hbar\omega_e$ and χ_e are the vibration quantum number, equilibrium vibrational energy, and anharmonicity constant. The obtained values are $\hbar\omega_e$= 78.45 ± 3.83 mV, χ_e = 1.1 × 10^{-2} ± 8.2 × 10^{-3} in R^2=0.9997 and predicted energy for vibrationally excited state are

summarized in Table 1. Parameters for $O_2[\bar{1}10]$ is obtained by the same method, which are $\hbar\omega_e= 93.33 \pm 2.30$ mV, $\chi_e = 2.6 \times 10^{-2} \pm 3.8 \times 10^{-3}$ in $R^2=0.9998$ and predicted energy for vibrationally excited state also in Table 1.
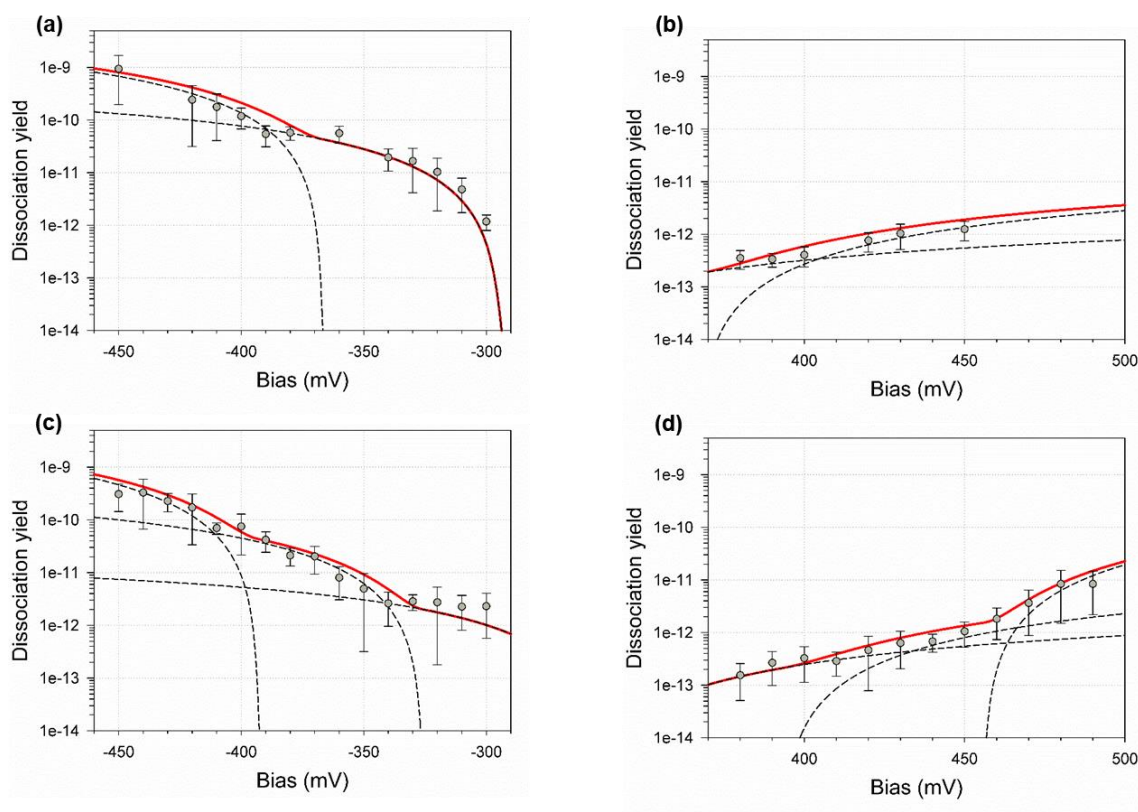
Figure 4.5. STM-AS of $O_2[\bar{1}10]$ and $O_2[001]$ which are (a)&(b) and (c)&(d), respectively. The black dotted line is fitting curve of AS to understand related reaction mode. The red solid line is for total reaction AS.

Moreover, we measured rate R(I) by tracing the current which can demonstrate the power-law dependence on I and n, R(I) $\propto$ I^n, describing n as how many electrons required for an event.[43,102,103] From the current dependency, R(I), in Fig. 4.6, estimated the reaction orders were 2.24 (2.18) and 1.97 (2.01) at 320 mV and 430 mV bias conditions for $O_2[001]$ ($O_2[\bar{1}10]$), respectively. These results imply that dissociation

reaction underwent by two electron process of vibration energy of 4th and 5th excited state ($E_{v0\rightarrow4}$= 294.0 (326.0) mV and $E_{v0\rightarrow5}$= 367.0 (393.0) mV from fitting data in AS) because the only lower quantized vibrational excited state can be activated by the injecting energy.

Table 1.

	$O_2[001]$ Exp.	Predicted	$O_2[\bar{1}10]$ Exp.	Predicted
$\nu = 1$	78.8 mV	76.7 mV	87.2 mV	88.5 mV
$\nu = 4$	294.0 mV	296.1 mV	326.0 mV	324.7 mV
$\nu = 5$	367.0 mV	365.7 mV	393.0 mV	393.8 mV
R^2		0.9998		0.9999
$\hbar\omega_e$		78.45 $\pm$ 3.83 mV		93.33 $\pm$ 2.30 mV
χ_e		1.1×10^{-2} $\pm 8.2 \times 10^{-3}$		2.6×10^{-2} $\pm 3.8 \times 10^{-3}$

The dissociation barrier was determined that 367 mV < gap < 588 mV for $O_2[001]$ and 400 mV < gap < 502 mV for $O_2[\bar{1}10]$. The multi-electron process goes through overtone excitations to exceed the reaction barrier for the dissociation of O_2 along [001] and [$\bar{1}10$]. Schematic description represents in Figure 4.7. The overtone of O-O stretch's 3rd, 4th, and 5th vibrationally excited reaction by two electron process lead the dissociation reaction toward [001] and [$\bar{1}10$] directions having different vibration energy.

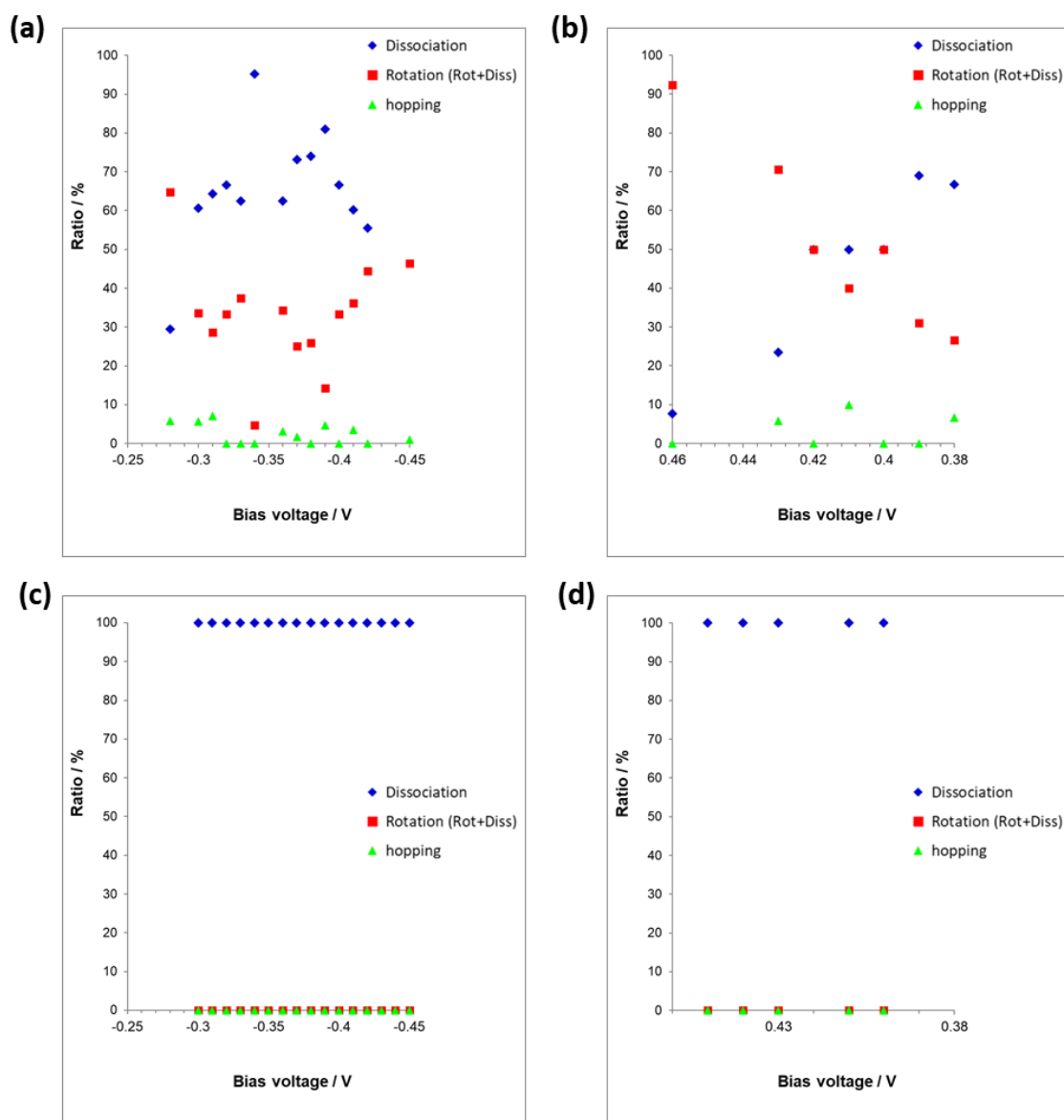**Figure 4.5.** Current dependency for $O_2[001]$ in (a) and (b). The (c) and (d) for $O_2[\bar{1}10]$ at both negative and positive bias voltage.
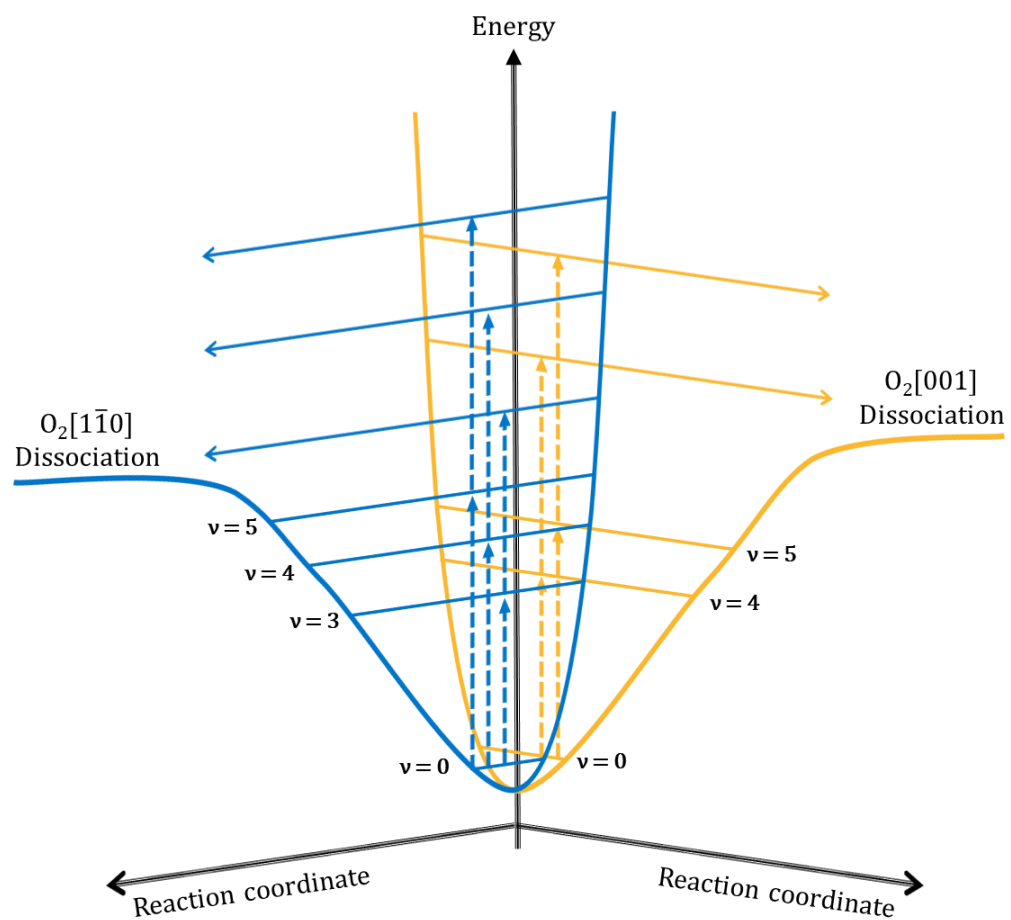
Figure 4.5. Schematic potential energy surface for vibrationally excited dissociation reaction for two directions.

3.2.4. Conclusion

In conclusion, we conducted the STM experiment under low temperature and ultrahigh vacuum condition for dissociation of chemisorbed O_2 on Ag(110) surface, in which traced the chemical reaction and revealed the mechanism by STM-IETS and STM-AS. There are two chemisorbed O_2 states along with the two surface lattice directions, $[\bar{1}10]$ and [001], and we verified the reaction pathways for each chemisorbed O_2 states. The rotation reaction was bidirectional and dissociation happened along their adsorbed direction. It is important that we identified the (O-O) vibrational mode for both $[\bar{1}10]$ and [001] O_2 molecules for the first time and anticipate the reaction gap by revealing the dissociation mechanism. The reaction induced by an overtone of vibrational excitation. We believe that this study provides the insight to oxidation reaction on the catalyst and helps to understand on-surface reaction investigation at a single molecular level.

4. Conclusion

The investigation of modifying the surface and monitoring the chemical reaction on surface, especially on metal surface, are of great interest that there are many previous studies. The metal surface is the common for catalyst which has reactivity for chemical reaction. To understand the cause of the reaction and to adjust surface properties, we handle two different topics in atomic-level studies using DFT calculation and STM experiments combined with IETS and AS.

In the first chapter, we discover the existence of highly-ordered hydroxylation of graphene/Cu(111) and explain it's of the superstructure. The graphene/Cu(111) surface exposed to -OH groups and forms the superstructure which maintained while the scale increase from the microscopic to the macroscopic range. This observed superstructure was calculated by DFT calculation. The optimized structures and DOS results show $C_6(OH)_1$ superstructure has high stability as experimentally observed due to strong -OH adsorption compared with other structures. In chapter two, we revealed the mechanism of O_2 dissociation on Ag(110) using combined STM, IETS, and AS experiments at atomic resolution. Possible reactions are studied by scanning the surface injecting the hot hole/electron to the O_2 molecules. STM-IETS is able to detect the rotation and vibration energy of the model system that we discovered the O-O vibration mode at ±78.8 mV for $O_2[001]$, ±87.2 mV for $O_2[\bar{1}10]$. These energy values are also shown in STM-AS which indicate the reaction induced by vibrational excitation. We conclude that this reaction occurs through overtone excitation of O_2 stretching mode and this study gives insights into O_2 dissociation on Ag(110).

Despite my works cover the small part of wide surface chemistry, we demonstrated that representative fundamental chemical reactions on surface. Moreover, the computational calculation is complementary to experimental studies that we expect co-works are helpful for revel the reaction with regard to surface chemistry.

5. Reference

1   Martin, R. M. *Electronic Structure: Basic Theory and Practical Methods*.   (Cambridge University Press, 2004).

2   Jensen, F. *Introduction to computational chemistry*.   (Wiley, 1999).

3   Szabo, A. & Ostlund, N. S. *Modern Quantum Chemistry: Introduction to Advanced Electronic Structure Theory*.   (Dover Publications, 1996).

4   Chen, C. J. *Introduction to scanning tunneling microscopy*.   (Oxford University Press, 1993).

5   Born, M. & Oppenheimer, R. On the quantum theory of molecules. *Annalen der Physik* **84**, 457-484 (1927).

6   Fock, V. Näherungsmethode zur Lösung des quantenmechanischen Mehrkörperproblems. *Zeitschrift für Physik* **61**, 126-148 (1930).

7   Slater, J. C. The theory of complex spectra. *Physical Review* **34**, 1293 (1929).

8   Møller, C. & Plesset, M. S. Note on an approximation treatment for many-electron systems. *Physical Review* **46**, 618 (1934).

9   Bartlett, R. J. Many-body perturbation theory and coupled cluster theory for electron correlation in molecules. *Annual Review of Physical Chemistry* **32** (1981).

10   Bartlett, R. J. Coupled-cluster approach to molecular-structure and spectra - a step toward predictive quantum-chemistry. *J Phys Chem-Us* **93**, 1697-1708 (1989).

11   Kohn, W. & Sham, L. J. Self-consistent qquations including exchange and correlation effects. *Physical Review* **140** (1965).

12   Parr, R. G. & Yang, W. *Density-functional theory of atoms and molecules*.   (Oxford University Press, 1989).

13   Hohenberg, P. & Kohn, W. Inhomogeneous electron gas. *Physical Review* **136** (1964).

14   Becke, A. D. Density-functional exchange-energy approximation with correct asymptotic-behavior. *Phys Rev A* **38**, 3098-3100 (1988).

15   Perdew, J. P. & Wang, Y. Accurate and simple analytic representation of the electron-gas correlation-energy. *Phys Rev B* **45**, 13244-13249 (1992).

16   Perdew, J. P. *et al.* Atoms, molecules, solids, and surfaces - applications of the generalized gradient approximation for exchange and correlation. *Phys Rev B* **46**, 6671-6687 (1992).

17   Perdew, J. P., Burke, K. & Ernzerhof, M. Generalized gradient approximation made simple. *Phys Rev Lett* **77**, 3865-3868 (1996).

18   Blochl, P. E., Jepsen, O. & Andersen, O. K. Improved tetrahedron method for Brillouin-

Zone integrations. *Phys Rev B* **49** (1994).

19   Kresse, G. & Joubert, D. From ultrasoft pseudopotentials to the projector augmented-wave method. *Phys Rev B* **59**, 1758-1775 (1999).

20   Kresse, G. & Hafner, J. Ab initio molecular dynamics for liquid metals. *Phys Rev B* **47**, 558-561 (1993).

21   Kresse, G. & Furthmuller, J. Efficient iterative schemes for ab initio total-energy calculations using a plane-wave basis set. *Phys Rev B* **54**, 11169-11186 (1996).

22   Hafner, J. Ab-initio simulations of materials using VASP: Density-functional theory and beyond. *Journal of computational chemistry* **29**, 2044-2078 (2008).

23   Binning, G., Rohrer, H., Gerber, C. & Weibel, E. Tunneling through a controllable vacuum gap. *Appl Phys Lett* **40** (1982).

24   Binnig, G., Rohrer, H., Gerber, C. & Weibel, E. 7x7 reconstruction on Si(111) resolved in real space. *Phys Rev Lett* **50**, 120-123 (1983).

25   Binnig, G. & Rohrer, H. Scanning tunneling microscopy - from birth to adolescence. *Rev Mod Phys* **59**, 615-625 (1987).

26   Garcia, N. Theory of scanning tunneling microscopy and spectroscopy - Resolution, image and field states, and thin oxide layers. *Ibm J Res Dev* **30**, 533-542 (1986).

27   Coombs, J. H. & Pethica, J. B. Properties of vacuum tunneling currents: Anomalous barrier heights. *Ibm J Res Dev* **30**, 455-459 (1986).

28   Selloni, A., Carnevali, P., Tosatti, E. & Chen, C. D. Voltage-dependent scanning-tunneling microscopy of a crystal surface: Graphite. *Phys Rev B* **31** (1985).

29   Hla, S. W. Scanning tunneling microscopy single atom/molecule manipulation and its application to nanoscience and technology. *J Vac Sci Technol B* **23**, 1351-1360 (2005).

30   Eigler, D. M. & Schweizer, E. K. Positioning single atoms with a scanning tunneling microscope. *Nature* **344**, 524-526 (1990).

31   Bartels, L., Meyer, G. & Rieder, K. H. Basic steps of lateral manipulation of single atoms and diatomic clusters with a scanning tunneling microscope tip. *Phys Rev Lett* **79**, 697-700 (1997).

32   Eigler, D. M., Lutz, C. P. & Rudge, W. E. An atomic switch realized with the scanning tunneling microscope. *Nature* **352**, 600-603 (1991).

33   Stipe, B. C., Rezaei, M. A. & Ho, W. Single-molecule vibrational spectroscopy and microscopy. *Science* **280**, 1732-1735 (1998).

34   Sainoo, Y. *et al.* Excitation of molecular vibrational modes with inelastic scanning tunneling microscopy processes: Examination through action spectra of cis-2-butene on Pd(110). *Phys Rev Lett* **95** (2005).

35   Ho, W. Single-molecule chemistry. *J Chem Phys* **117**, 11033-11061 (2002).

36   Motobayashi, K., Kim, Y., Ueba, H. & Kawai, M. Insight into action spectroscopy for single molecule motion and reactions through inelastic electron tunneling. *Phys Rev Lett* **105** (2010).

37   Komeda, T., Kim, Y., Kawai, M., Persson, B. N. J. & Ueba, H. Lateral hopping of molecules induced by excitation of internal vibration mode. *Science* **295**, 2055-2058 (2002).

38   Pascual, J. I., Lorente, N., Song, Z., Conrad, H. & Rust, H. P. Selectivity in vibrationally mediated single-molecule chemistry. *Nature* **423**, 525-528 (2003).

39   Stipe, B. C., Rezaei, M. A. & Ho, W. Inducing and viewing the rotational motion of a single molecule. *Science* **279**, 1907-1909 (1998).

40   Stipe, B. C., Rezaei, M. A. & Ho, W. Coupling of vibrational excitation to the rotational motion of a single adsorbed molecule. *Phys Rev Lett* **81**, 1263-1266 (1998).

41   Kim, Y., Komeda, T. & Kawai, M. Single-molecule reaction and characterization by vibrational excitation. *Phys Rev Lett* **89** (2002).

42   Katano, S., Kim, Y., Hori, M., Trenary, M. & Kawai, M. Reversible control of hydrogenation of a single molecule. *Science* **316**, 1883-1886 (2007).

43   Stipe, B. C. *et al.* Single-molecule dissociation by tunneling electrons. *Phys Rev Lett* **78**, 4410-4413 (1997).

44   Ohara, M., Kim, Y., Yanagisawa, S., Morikawa, Y. & Kawai, M. Role of molecular orbitals near the Fermi level in the excitation of vibrational modes of a single molecule at a scanning tunneling microscope junction. *Phys Rev Lett* **100** (2008).

45   Shin, H. J. *et al.* State-selective dissociation of a single water molecule on an ultrathin MgO film. *Nature materials* **9**, 442-447 (2010).

46   Ohara, M., Kim, Y. & Kawai, M. Electric field response of a vibrationally excited molecule in an STM junction. *Phys Rev B* **78** (2008).

47   Paulsson, M., Frederiksen, T., Ueba, H., Lorente, N. & Brandbyge, M. Unified description of inelastic propensity rules for electron transport through nanoscale junctions. *Phys Rev Lett* **10** (2008).

48   Motobayashi, K., Quantitative understanding of single molecular motion and reaction through inelastic electron tunneling by STM, Ph.D.Thesis thesis, The University of Tokyo, (2010).

49   Ueba, H., Mii, T. & Tikhodeev, S. G. Theory of inelastic tunneling spectroscopy of a single molecule - Competition between elastic and inelastic current. *Surf Sci* **601**, 5220-5225 (2007).

50   Lorente, N. & Persson, M. Theory of single molecule vibrational spectroscopy and

microscopy. *Phys Rev Lett* **85**, 2997-3000 (2000).

51   Allen, M. J., Tung, V. C. & Kaner, R. B. Honeycomb Carbon: A Review of Graphene. *Chemical reviews* **110**, 132-145 (2010).

52   Geim, A. K. & Novoselov, K. S. The rise of graphene. *Nature materials* **6**, 183-191 (2007).

53   Son, Y. W., Cohen, M. L. & Louie, S. G. Energy gaps in graphene nanoribbons. *Phys Rev Lett* **97** (2006).

54   Han, M. Y., Ozyilmaz, B., Zhang, Y. B. & Kim, P. Energy band-gap engineering of graphene nanoribbons. *Phys Rev Lett* **98** (2007).

55   Ruffieux, P. *et al.* On-surface synthesis of graphene nanoribbons with zigzag edge topology. *Nature* **531**, 489 (2016).

56   Lim, H., Jung, J., Ruoff, R. S. & Kim, Y. Structurally driven one-dimensional electron confinement in sub-5-nm graphene nanowrinkles. *Nature communications* **6**, 8601 (2015).

57   Bai, J. W., Zhong, X., Jiang, S., Huang, Y. & Duan, X. F. Graphene nanomesh. *Nat Nanotechnol* **5**, 190-194 (2010).

58   Elias, D. C. *et al.* Control of Graphene's Properties by Reversible Hydrogenation: Evidence for Graphane. *Science* **323**, 610-613 (2009).

59   Ni, Z. H. *et al.* On Resonant Scatterers As a Factor Limiting Carrier Mobility in Graphene. *Nano Lett* **10**, 3868-3872 (2010).

60   Ryu, S. *et al.* Reversible Basal Plane Hydrogenation of Graphene. *Nano Lett* **8**, 4597-4602 (2008).

61   Balog, R. *et al.* Atomic Hydrogen Adsorbate Structures on Graphene. *J Am Chem Soc* **131**, 8744 (2009).

62   Guisinger, N. P., Rutter, G. M., Crain, J. N., First, P. N. & Stroscio, J. A. Exposure of Epitaxial Graphene on SiC(0001) to Atomic Hydrogen. *Nano Lett* **9**, 1462-1466 (2009).

63   Hossain, M. Z. *et al.* Chemically homogeneous and thermally reversible oxidation of epitaxial graphene. *Nat Chem* **4**, 305-309 (2012).

64   Robinson, J. T. *et al.* Properties of Fluorinated Graphene Films. *Nano Lett* **10**, 3001-3005 (2010).

65   Lee, W. H. *et al.* Selective-Area Fluorination of Graphene with Fluoropolymer and Laser Irradiation. *Nano Lett* **12**, 2374-2378 (2012).

66   Gan, L. *et al.* Tuning the properties of graphene using a reversible gas-phase reaction. *Npg Asia Mater* **4** (2012).

67   Sofo, J. O., Chaudhari, A. S. & Barber, G. D. Graphane: A two-dimensional hydrocarbon. *Phys Rev B* **75** (2007).

68   Yan, J. A., Xian, L. D. & Chou, M. Y. Structural and Electronic Properties of Oxidized

Graphene. *Phys Rev Lett* **103** (2009).

69   Klimes, J., Bowler, D. R. & Michaelides, A. Van der Waals density functionals applied to solids. *Phys Rev B* **83** (2011).

70   Li, X. *et al.* Influence of water on the electronic structure of metal-supported graphene: Insights from van der Waals density functional theory. *Phys Rev B* **85** (2012).

71   Csonka, G. I. *et al.* Assessing the performance of recent density functionals for bulk solids. *Phys Rev B* **79** (2009).

72   Giovannetti, G. *et al.* Doping graphene with metal contacts. *Phys Rev Lett* **101** (2008).

73   Gong, C. *et al.* First-principles study of metal-graphene interfaces. *J Appl Phys* **108** (2010).

74   Momma, K. & Izumi, F. VESTA 3 for three-dimensional visualization of crystal, volumetric and morphology data. *J Appl Crystallogr* **44**, 1272-1276 (2011).

75   Jung, J., Lim, H., Oh, J. & Kim, Y. Functionalization of Graphene Grown on Metal Substrate with Atomic Oxygen: Enolate vs Epoxide. *J Am Chem Soc* **136**, 8528-8531 (2014).

76   Hormandinger, G. Imaging of the Cu(111) Surface-State in Scanning-Tunneling-Microscopy. *Phys Rev B* **49**, 13897-13905 (1994).

77   Diekhoner, L. *et al.* Surface states of cobalt nanoislands on Cu(111). *Phys Rev Lett* **90** (2003).

78   Gao, L., Guest, J. R. & Guisinger, N. P. Epitaxial Graphene on Cu(111). *Nano Lett* **10**, 3512-3516 (2010).

79   Campbell, C. T. & Paffett, M. T. Model Studies of Ethylene Epoxidation Catalyzed by the Ag(110) Surface. *Surf Sci* **139**, 396-416 (1984).

80   Serafin, J. G., Liu, A. C. & Seyedmonir, S. R. Surface science and the silver-catalyzed epoxidation of ethylene: an industrial perspective. *J Mol Catal a-Chem* **131**, 157-168 (1998).

81   Gravil, P. A., Bird, D. M. & White, J. A. Adsorption and Dissociation of O2 on Ag(110). *Physical review letters* **77**, 3933-3936 (1996).

82   Olsson, F. E., Lorente, N. & Persson, M. STM images of molecularly and atomically chemisorbed oxygen on silver. *Surf Sci* **522**, L27-L35 (2003).

83   Barth, J. V., Zambelli, T., Wintterlin, J., Schuster, R. & Ertl, G. Direct observation of mobility and interactions of oxygen molecules chemisorbed on the Ag(110) surface. *Phys Rev B* **55**, 12902-12905 (1997).

84   Gravil, P. A., White, J. A. & Bird, D. M. Chemisorption of O2 on Ag(110). *Surf Sci* **352**, 248-252 (1996).

85   Bird, D. M. & Gravil, P. A. First-principles calculations of molecular dissociation at

surfaces. *Surf Sci* **377**, 555-562 (1997).

86   Hahn, J. R., Lee, H. J. & Ho, W. Electronic resonance and symmetry in single-molecule inelastic electron tunneling. *Phys Rev Lett* **85**, 1914-1917 (2000).

87   Hahn, J. R. & Ho, W. Chemisorption and dissociation of single oxygen molecules on Ag(110). *J Chem Phys* **123** (2005).

88   Hahn, J. R. & Ho, W. Orbital specific chemistry: controlling the pathway in single-molecule dissociation. *J Chem Phys* **122**, 244704 (2005).

89   Hahn, J. R., Jang, S. H., Kim, K. W. & Son, S. B. Hot carrier-selective chemical reactions on Ag(110). *J Chem Phys* **139** (2013).

90   Sharani Roy, V. M., and Mark A. Ratner. Chemistry at molecular junctions: Rotation and dissociation of O2 on the Ag(110) surface induced by a scanning tunneling microscope. *The Journal of Chemical Physics* **139**, 074702 (2013).

91   Rawal, T. B., Hong, S., Pulkkinen, A., Alatalo, M. & Rahman, T. S. Adsorption, diffusion, and vibration of oxygen on Ag(110). *Phys Rev B* **92** (2015).

92   Loncaric, I., Alducin, M. & Juaristi, J. I. Molecular dynamics simulation of O2 adsorption on Ag(110) from first principles electronic structure calculations. *Physical chemistry chemical physics : PCCP* **18**, 27366-27376 (2016).

93   Loncaric, I., Alducin, M., Saalfrank, P. & Juaristi, J. I. Femtosecond-laser-driven molecular dynamics on surfaces: Photodesorption of molecular oxygen from Ag(110). *Phys Rev B* **93** (2016).

94   Loncaric, I., Alducin, M. & Juaristi, J. I. Dissociative dynamics of O2 on Ag(110). *Physical chemistry chemical physics : PCCP* **17**, 9436-9445 (2015).

95   Vattuone, L. *et al.* Azimuthal Dependence of Sticking Probability of O2 on Ag(110). *Phys Rev Lett* **72**, 510-513 (1994).

96   Vattuone, L., Rocca, M., Boragno, C. & Valbusa, U. Initial Sticking Coefficient of O2 on Ag(110). *J Chem Phys* **101**, 713-725 (1994).

97   Raukema, A., Butler, D. A. & Kleyn, A. W. The interaction of oxygen with the Ag(110) surface. *J Phys-Condens Mat* **8**, 2247-2263 (1996).

98   Bartolucci, F., Franchy, R., Barnard, J. C. & Palmer, R. E. Two Chemisorbed Species of O_2 on Ag(110). *Phys Rev Lett* **80**, 5224-5227 (1998).

99   Oh, J. *et al.* Lateral Hopping of CO on Ag(110) by Multiple Overtone Excitation. *Phys Rev Lett* **116** (2016).

100   Hahn, J. R. & Ho, W. Single molecule imaging and vibrational spectroscopy with a

chemically modified tip of a scanning tunneling microscope. *Phys Rev Lett* **87** (2001).

101   Monturet, S., Alducin, M. & Lorente, N. Role of molecular electronic structure in inelastic electron tunneling spectroscopy: O_2 on Ag(110). *Phys Rev B* **82** (2010).

102   Stipe, B. C., Rezaei, M. A. & Ho, W. Inducing and viewing the rotational motion of a single molecule. *Science* **279**, 1907-1909 (1998).

103   Kim, Y., Komeda, T. & Kawai, M. Single-Molecule Reaction and Characterization by Vibrational Excitation. *Phys Rev Lett* **89**, 126104 (2002).

Appendix. Bibliography

Publication

1. S. Kim, C. Park, **M. Lee**, I. Song, J. Kim, M. Lee, J. Jung, Y. Kim, H. Lim*, and H. C. Choi*, Rapid photochemical synthesis of sea-urchin-shaped hierarchical porous COF-5 and its lithography-free patterned growth. Adv. Funct. Mater. 27(32), 1700925 (2017).

2. **M. Lee**, J. Jung*, and Y. Han*, Understanding dimerization process of cyclohexyl benzene as an overcharge protection agent in lithium ion battery. Bull. Korean Chem. Soc. 39(10), 1227-1230 (2018).

3. S. Sivan (§), **M. Lee (§)**, S.-K. Lee (§), J.-W. Yoon, D. Y. Hong, K.-H. Cho, U-H. Lee, J.-S. Chang*, J. Jung*, and Y. K. Hwang*, Molecular encapsulation of trimeric chromium carboxylate cluster in metal-organic frameworks and propylene sorption. Chem. Eur. J. submitted (2019) (§Equally contributing authors)

4. H. Lim, Y. H. Park, **M. Lee**, J.-G. Ahn, B. W. Li, J. Jung,* and R. S. Ruoff,* and Y. Kim,* Periodic Hydroxylation of Single Crystal Graphene: Highly Crystalline $C_6(OH)_1$, in preparation

5. **M. Lee**, E. Kazuma, C. Zhang, J. Jung,* and Y. Kim,* Electron-induced dissociation of O_2 on Ag(110), in preparation

Presentation

1. <u>Minhui Lee</u>, Sung Hwan Mun, Hyunseob Lim*, Jaehoon Jung*, and Yousoo Kim*, Computational study on the formation of a highly-ordered hydroxylated graphene epitaxially-grown on Cu(111). Poster, IIRC-5 (The 5th Ito International Research Conference), Tokyo, Japan, Nov. 20-23, 2017

2. <u>Minhui Lee</u>, Hyunseob Lim*, Jaehoon Jung*, and Yousoo Kim*, Highly-ordered hydroxylated graphene epitaxially grown on Cu(111). Poster, ACSIN-

14 (The 14th International Conference on Atomically Controlled Surfaces, Interfaces, and Nanostructures), Sendai, Japan, Oct. 21-25, 2018

Honor

1. International Program Associate (IPA) scholarship, Surface and Interface Science Laboratory (PI: Dr. Yousoo Kim), RIKEN, Japan (2018.02-2019.01)